

A Deep X-ray Survey of the Globular Cluster Omega Centauri

Simon Henleywillis,¹★ Adrienne M. Cool,²† Daryl Haggard,³ Craig Heinke,⁴
Paul Callanan,¹ and Yue Zhao⁴

¹Department of Physics, University College Cork, College Road, Cork, Ireland

²Department of Physics and Astronomy, San Francisco State University, 1600 Holloway Avenue, San Francisco, CA 94132, USA

³McGill Space Institute, 3550 University Street, Montreal, QC H3A 2A7, Canada

⁴Department of Physics, University of Alberta, CCIS 4-183, Edmonton, AB T6G 2E1, Canada

Last updated 2015 May 22; in original form 2013 September 5

ABSTRACT

We identify 233 X-ray sources, of which 95 are new, in a 222 ks exposure of Omega Centauri with the *Chandra X-ray Observatory*’s ACIS-I detector. The limiting unabsorbed flux in the core is $f_X(0.5\text{--}6.0\text{ keV}) \approx 3 \times 10^{-16}\text{ erg s}^{-1}\text{ cm}^{-2}$ ($L_X \approx 1 \times 10^{30}\text{ erg s}^{-1}$ at 5.2 kpc). We estimate that $\sim 60 \pm 20$ of these are cluster members, of which ~ 30 lie within the core ($r_c = 155\text{ arcsec}$), and another ~ 30 between 1–2 core radii. We identify four new optical counterparts, for a total of 45 likely identifications. Probable cluster members include 18 cataclysmic variables (CVs) and CV candidates, one quiescent low-mass X-ray binary, four variable stars, and five stars that are either associated with ω Cen’s anomalous red giant branch, or are sub-subgiants. We estimate that the cluster contains 40 ± 10 CVs with $L_X > 10^{31}\text{ erg s}^{-1}$, confirming that CVs are underabundant in ω Cen relative to the field. Intrinsic absorption is required to fit X-ray spectra of six of the nine brightest CVs, suggesting magnetic CVs, or high-inclination systems. Though no radio millisecond pulsars (MSPs) are currently known in ω Cen, more than 30 unidentified sources have luminosities and X-ray colours like those of MSPs found in other globular clusters; these could be responsible for the *Fermi*-detected gamma-ray emission from the cluster. Finally, we identify a CH star as the counterpart to the second-brightest X-ray source in the cluster and argue that it is a symbiotic star. This is the first such giant/white dwarf binary to be identified in a globular cluster.

Key words: novae, cataclysmic variables – X-rays: binaries – globular clusters: individual (ω Centauri) – binaries: close

1 INTRODUCTION

Significant progress has been made in recent years in unraveling the complex interplay between stellar dynamics and stellar evolution in globular clusters (e.g. Wang et al. 2016; Rodriguez et al. 2016). On the observational side, critical insights have come from X-ray imaging, which reveals many of the binary stars that drive cluster evolution at late times. The nearest globular clusters are prime targets for such studies. For these clusters, long exposures with the *Chandra X-ray Observatory* can sample luminosities as faint as $L_X \sim 10^{30}\text{ erg s}^{-1}$, which enables compilation of near-complete samples of compact binaries (e.g. Grindlay et al. 2001; Pooley et al. 2003; Heinke et al. 2005). *Chandra* also brings within reach significant numbers of main-sequence and/or subgiant binaries that reveal themselves through enhanced coronal activity (e.g. Bassa et al. 2004; Cohn et al. 2010).

Among nearby clusters, ω Cen stands out. It is the most luminous of our Galaxy’s globular clusters ($M_V = -10.26$; Harris 2010) and, with a mass of $\sim 3 \times 10^6 M_\odot$ (D’Souza & Rix 2013; Baumgardt 2017), is the second most massive globular cluster in the entire Local Group. Well-fit by a King-Michie model (Trager et al. 1995; Ferraro et al. 2006), it has an enormous core with radius $r_c \approx 155\text{ arcsec} = 3.9\text{ pc}$ at an assumed distance of 5.2 kpc (Trager et al. 1995; Harris 2010). As a result, a high rate of stellar interactions is predicted (Verbunt & Meylan 1988; Di Stefano & Rappaport 1994; Davies & Benz 1995), despite the cluster’s relatively modest central density ($\rho_0 \sim 3 \times 10^3 M_\odot/\text{pc}^3$; Pryor & Meylan 1993).

Omega Cen was also the first cluster to show signs of multiple stellar populations (Freeman & Rodgers 1975; Norris & Da Costa 1995; Anderson 2002), a phenomenon now well-documented in nearly every closely-examined globular cluster in the Milky Way (Piotto et al. 2015). In ω Cen’s case, the spread in chemical composition is unusually large, and includes widely disparate Fe abundances among its multiple populations (see review by Gratton et al. 2004). These curious properties have led to the suggestion that

★ Contact e-mail: s.henleywillis@mars.ucc.ie

† Contact e-mail: cool@sfsu.edu

ω Cen may not be a globular cluster at all, but instead the remnant nucleus of a dwarf galaxy captured by the Milky Way (Norris et al. 1996; Lee et al. 1999; Bekki & Freeman 2003).

Observations with successive generations of X-ray observatories have revealed increasingly large numbers of sources in and toward ω Cen. Five were found with *Einstein/IPC* (Hertz & Grindlay 1983), 21 with *ROSAT/SPPC* (Johnston et al. 1994; Verbunt & Johnston 2000), and 146 with *XMM-Newton* (Gendre et al. 2003). In each case, roughly one third to one-half of the sources lay within about 3 core radii of the cluster centre, where membership in the cluster becomes more probable. The first *Chandra* observation of ω Cen, a ~ 70 ksec exposure with the Advanced CCD Imaging Spectrometer’s imaging array (ACIS-I), expanded the number of X-ray sources to 180, ~ 150 of which lie interior to $3r_c$ (Haggard et al. 2009, see also Cool et al. 2002).

The ability to observe faint stars even in the cluster core with the *Hubble Space Telescope* (*HST*) has made it possible to identify optical counterparts for a significant number of these sources (Carson et al. 2000; Haggard et al. 2004; Cool et al. 2013). Optical counterparts are essential for classifying the objects that are responsible for the X-ray emission; very few objects can be uniquely identified on the basis of X-rays alone, quiescent low-mass X-ray binaries being a rare exception (Rutledge et al. 2002). Innovations in ground-based photometric techniques have also uncovered a large number of variable stars in ω Cen (Kaluzny et al. 1996, 2004), some of which are detectable in X-rays at the sensitivity levels achieved by *XMM-Newton* and *Chandra*.

In 2012 we obtained a second epoch of *Chandra* imaging of ω Cen. A primary goal of the study, which had a factor of about three more exposure time than the original study, was to search for – or put limits on – X-ray emission from a potential intermediate-mass black hole (IMBH). Focusing on the central part of the ACIS-I field of view, we found no X-ray emission coincident with the cluster centre, and concluded that if an IMBH does exist in ω Cen then it must be experiencing very little or very inefficient accretion (Haggard et al. 2013).

Here we report our analysis of the full 2012 ACIS-I ω Cen dataset. In Section 2 we describe the observations, how we processed the data, and the methods by which we identified sources and measured their properties. We compare the results to those obtained from the first epoch of observations in Section 3. In Section 4 we compare the observed sources to predicted numbers of active galactic nuclei (AGN) and X-ray-detectable foreground stars both to determine how many sources are cluster members and to assess their radial and luminosity distribution. In Section 5 we summarise existing optical identifications and add several more by comparing the new source list to existing catalogues of variable stars. A particularly interesting new optical ID, the first symbiotic star found in a globular cluster, is described in Section 6. In Section 7 we present an X-ray colour–magnitude diagram along with spectral and timing analyses of several of the brightest sources in the cluster (additional spectral and timing analyses will appear elsewhere). We discuss the findings in Section 8 and summarise them in Section 9.

2 X-RAY OBSERVATIONS AND SOURCE LIST

We obtained two long exposures of ω Cen using the imaging array of the *Chandra X-ray Observatory*’s Advanced CCD Imaging Spectrometer (ACIS-I) on 2012 April 16–17. The datasets have a combined exposure time of ~ 222 ksec (173.7 and 48.5 ksec for ObsIDs 13726 and 13727, respectively). The cluster centre was placed

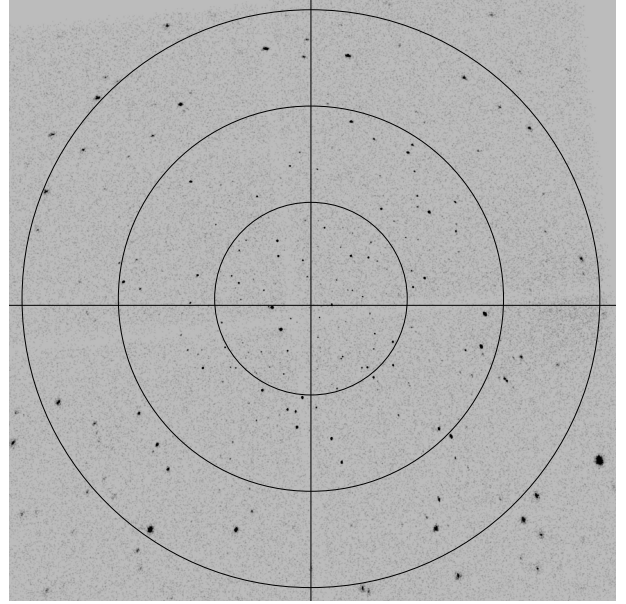


Figure 1. Smoothed 222 ksec *Chandra* ACIS-I image of ω Cen. Circles indicate 1, 2, and 3 core radii ($r_c = 155$ arcsec), and the crosshair indicates the cluster centre. The cluster’s half-mass radius is 5.0 arcmin, i.e. just under 2 core radii.

near the middle of the imaging array’s $\sim 16.9 \times 16.9$ arcmin field of view (see Fig. 1), which is comprised of a 2×2 array of 1024×1024 chips with ~ 0.49 arcsec pixels. To optimise the detection of faint sources, we used the ‘very faint’ telemetry format in the Timed Exposure mode, which permits improved screening for particle events in post-processing¹.

We processed the two raw datasets using CIAO’s `CHANDRA_REPRO`. This tool filters events by grade and status, selects good time intervals, and generates a bad pixel file. Reprocessing also enabled us to take advantage of the ‘very faint’ mode and flag events associated with cosmic rays, which significantly reduced the background rate in the final level=2 event files. In preparation for source detection, we combined the two level=2 events files using `MERGE_OBS` to create an unbinned merged image in the 0.5–4.5 keV band for the full dataset. Eliminating counts above 4.5 keV at this stage further reduced the background with relatively little effect on the counts associated with most sources. This tool also generated an exposure map suitable for use with `WAVDETECT` (see below). We generated a point spread function (PSF) map at 1.9 keV for an encircled counts fraction (ECF) of 0.5. Since PSF maps cannot be generated directly for merged images, we first created separate PSF maps for each ObsID and then used `DMIMGCALC` to produce an exposure-weighted sum of the two. The choice of ECF=0.5 was made after experimenting with `WAVDETECT` and finding that the ability to distinguish closely-spaced on-axis sources was sensitive to this parameter.

We used CIAO’s `WAVDETECT` tool to search for sources in the 0.5–4.5 keV merged image, supplying it with the exposure map and PSF map described above. After experimenting with various combinations of parameters, we adopted wavelet scales [1, 2, 4, 8] and a source significance threshold of 10^{-6} . This set of

¹ See <http://cxc.cfa.harvard.edu/proposer/POG/html/chap6.html>

Table 1. Adopted aperture radii and background annuli.

Offset (arcminutes)	Aperture Radius (pixels)	Background Annulus (pixels)
<4	4	15–30
4–5	6	15–30
5–6	8	15–30
6–7	10	30–45
7–9.5	12	30–45
>9.5	14	30–45

parameters was effective at picking up close pairs inside the half-mass radius while limiting spurious off-axis sources.

Table 3 lists the full set of 233 sources that appear in the 2012 data set, 95 of which are new. We adopt the same labelling convention used by Haggard et al. (2009), who identified 180 sources in the first epoch of *Chandra* data, 138 of which are recovered here (see Section 3). For new sources, we assign a three-character ID based on radial offset from the centre of the cluster² and azimuthal angle (see column 1 of Table 3). The first character is a number between 1 and 10 equal to the radial offset rounded to 1 arcmin. The second character is a number between 1 and 4 identifying the quadrant in which the source falls. The third character is a letter based on azimuthal angle, increasing counterclockwise. Original labels were kept for re-detected sources; new source names begin with the next available letter and are shown in bold face. Coordinates for the sources, as reported by WAVDETECT, are given in column 2 of Table 3. Uncertainties on these positions, at 95 per cent confidence, computed from WAVDETECT source counts and off-axis angle following the empirical formula developed by Hong et al. (2005, see their Eq. 5), are listed in column 3. Radial offsets from the cluster centre in units of the core radius ($r_c = 155$ arcsec) are listed in column 4. For these offsets we adopted the centre measured by Anderson & van der Marek (2010): R.A. = $13^h 26^m 47^s 24$, Dec. = $-47^\circ 28' 46'' 45$.

To determine source counts and fluxes we used the CIAO tool SRCFLUX. We extracted counts in apertures that increase in size with increasing distance from the optical axis to ensure encircled energies ≥ 50 per cent at 1.9 keV over the full field (and ≥ 80 per cent for most sources; see Table 1). For purposes of comparison to Haggard et al. (2009) and to long-exposure *Chandra* studies of other nearby globular clusters (e.g. Heinke et al. 2005; Bogdanov et al. 2010), we extracted counts in several bands: ‘medium’ (0.5–4.5 keV), ‘soft’ (0.5–1.5 keV), ‘hard’ (1.5–6.0 keV), ‘wide’ (0.5–6.0 keV), as well as in the 0.5–2.0 keV soft band used for the *Chandra* Deep Field South (CDF-S; Luo et al. 2008). The first numbers listed in the columns 5–7 of Table 3 are the merged raw counts in the first three of these bands. We note that SRCFLUX does not operate on merged images; we therefore extracted raw source counts from the two level=2 events files individually and summed the results.

The second entries in columns 5–7 incorporate three adjustments to the raw counts: background subtraction, aperture correction, and an exposure correction. We measured background values for each source separately in annuli centred on the sources and sufficiently large to yield background values accurate to ~ 10 per cent and sufficiently far from the sources that no more than 3 per

cent of source counts fall in the annulus (and much less than 1 per cent in most cases; see Table 1). Several background annuli encompass a neighboring source; in these cases we excluded the imposing source’s region from the annulus before measuring the background level. A small number of faint sources for which background subtraction produced negative values in the soft or hard bands are listed in Table 3 as having zero corrected counts. Following background subtraction, we made aperture corrections by dividing the background-subtracted counts by the 1.9 keV encircled energy associated with each individual source, as reported by SRCFLUX. Finally, to correct for differing effective areas across the field (e.g. due to chip gaps), we normalised all sources to the typical on-axis value of 350 cm^2 . Corrected counts are thus given by:

$$\text{corrected counts} = \left(\frac{\text{NET_COUNTS}}{\text{PSFFRAC}} \right) \left(\frac{350 \text{ cm}^2}{\text{MEAN_SRC_EXP}} \right) \quad (1)$$

The log of the ratio of the corrected counts in the soft vs. hard bands is given in Table 3, column 8.

To convert corrected counts to unabsorbed fluxes we chose a power law model with a photon index of 1.4, appropriate for the large number of AGN expected to be included among the sources (see Section 4; Giacconi et al. 2001). We assumed a hydrogen column toward ω Cen of $n_H = 9 \times 10^{20} \text{ cm}^{-2}$. The latter was derived assuming $E(B-V) = 0.11$ (Lub 2002), $A_V/E(B-V) = 3.1$ (Cardelli et al. 1989), and $n_H/A_V = 2.81 \times 10^{21}$ (Bahramian et al. 2015). We used a Tuebingen-Boulder interstellar medium absorption model and abundances from Wilms et al. (2000) (see Heinke et al. 2014), which are incorporated into SRCFLUX as tbabs and wilm, respectively. The resulting unabsorbed fluxes for the medium, wide, and CDF-S soft bands are reported in Table 3 columns 9–11, respectively. These fluxes are exposure-time weighted averages of fluxes determined by running SRCFLUX on the two level=2 events files separately.

In Fig. 2 we plot the 0.5–4.5 keV fluxes from Table 3 for the 233 sources reported here against their radial offsets from the cluster centre, 20 arcsec from the ACIS-I aimpoint. The 138 recovered sources are shown as blue circles and the 95 new sources are shown as red triangles. Fluxes measured in the first-epoch data for 42 sources that were not recovered in the new data are shown as black dots. These bring the total number of X-ray sources known in and toward ω Cen to 275. The impact of the off-axis broadening of the PSF is clearly visible: while the limiting flux reaches $f_X(0.5\text{--}4.5 \text{ keV}) \sim 2 \times 10^{-16} \text{ erg s}^{-1}$ near the cluster centre, the limit increases steadily with radius, reaching $f_X(0.5\text{--}4.5 \text{ keV}) \sim 2 \times 10^{-15} \text{ erg s}^{-1}$ near the edge of the ACIS-I field.

3 COMPARISON WITH FIRST-EPOCH OBSERVATIONS

The field of view of the present observations overlaps with the first-epoch observations by approximately 88 per cent. In principle the two could be combined to yield a somewhat deeper image; however, given the significant change in sensitivity of ACIS-I in the ~ 12 yr time period separating the two observations and the strong wavelength dependence of those changes,³ characterization of the resulting sources would be problematic. Instead we compare results obtained by reducing the two epochs separately.

To ensure that we are making valid comparisons, we have re-extracted source counts and recomputed fluxes from the 2000 dataset using procedures identical to those used for the 2012 data,

² To preserve consistency with Haggard et al. (2009), we assigned source IDs using the same cluster centre adopted in that paper (R.A. = $13^h 26^m 45^s 89$, Dec. = $-47^\circ 28' 36'' 7$).

³ See <http://cxc.harvard.edu/ciao/why/acisqecontam.html> for details.

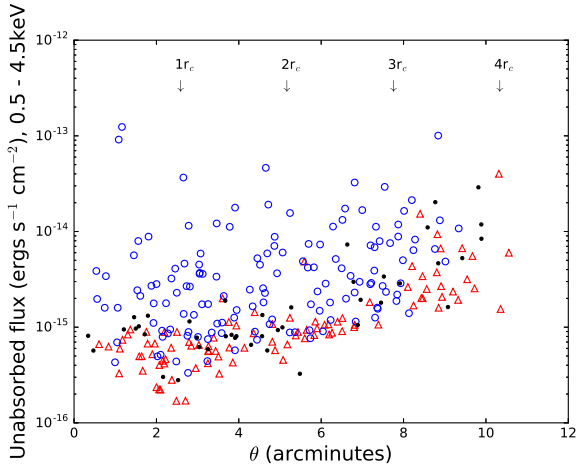


Figure 2. X-ray flux as a function of angular distance from the cluster centre for 275 known *Chandra* sources in and toward ω Cen. Red triangles represent 95 sources newly found in this study. Blue circles are 138 sources reported by Haggard et al. (2009) and recovered in the present study. Black dots are 42 sources found by Haggard et al. (2009) that were not detected in the 2012 dataset, including six that lie outside the ACIS-I field of view of the new data. Fluxes for these sources were remeasured from the 2000 dataset using methods identical to those used for the 2012 data.

beginning with the Haggard et al. (2009) source list. This is important given that the details of the analysis methods adopted here differ somewhat from those used by Haggard et al. (2009). In Fig. 3 we plot the 2012 0.5–6.0 keV fluxes as a function of the 2000 fluxes in the same band for sources that appear in both datasets. Ratios of these fluxes are also listed in column 12 of Table 3. Here it can be seen that while many sources have 2012 fluxes that are consistent with their values 12 years earlier (solid red line), a significant number have changed in brightness by a factor of 2–3. The median flux ratio for the full set of 138 sources is 0.94. A small number of sources show variations in excess of 3 and up to a factor of ~ 10 . The source with the largest change in flux is a known cataclysmic variable (CV; ID = 12a); its flux dropped by a factor of ~ 15 from 2000 to 2012.

The assumption of an identical spectrum for all sources in computing the fluxes (see Section 2) means that not all of the apparent flux changes seen in Fig. 3 will necessarily be indicative of actual source variability. Sources whose spectra differ significantly from the assumed $\Gamma = 1.4$ power-law spectrum will have different inferred fluxes in the absence of any real change in brightness owing to the change in sensitivity of the instrument as a function of wavelength in the 12 yr interval between the two sets of observations. Nevertheless, the fact that the median flux ratio for the full set of 138 sources is close to unity suggests that the spectral model we have adopted is reasonable for the bulk of the sources.

Further evidence for considerable flux variations for the sources in this field comes from the fact that 36, i.e. ~ 20 per cent, of the sources detected in 2000 are not detected in the 2012 data despite lying within the 2012 ACIS-I FOV (see Fig. 2). This is in spite of the fact that the exposure time for the 2012 observations is more than a factor of three longer than for the first-epoch observations (although the loss of sensitivity offsets the increased exposure time somewhat). Conversely, 82 of the sources reported here are in the earlier ACIS-I FOV but were not detected in that observation. While most of the latter are faint sources that would have been below the flux limit in the shorter exposures, others are

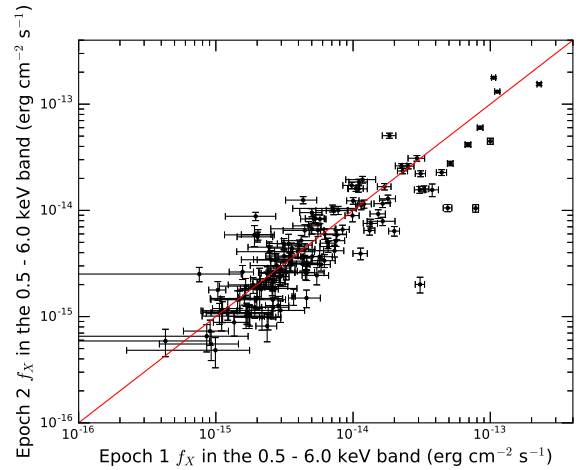


Figure 3. Unabsorbed wide-band 2012 fluxes vs. 2000 fluxes for the 138 sources that the two observations have in common. Fluxes have been derived assuming a power law with photon index $\Gamma = 1.4$ (see Section 3). The red line denotes equality. Error bars represent statistical uncertainties only and do not account for systematic errors associated with assuming a single spectral shape for all sources.

clearly bright enough that they should have been detected in the absence of intrinsic variation (see Fig. 2).

Variability in X-rays is characteristic of nearly all types of objects we expect to detect in these data, including cataclysmic variables and active binaries in the cluster, AGN in the background, and X-ray bright stars in the foreground; we analyse several of the brightest sources in Section 7 below. An exception is the quiescent neutron star (source 44e) in ω Cen (Rutledge et al. 2002; Gendre et al. 2003; Haggard et al. 2004). If this object is truly quiescent and is not accreting, then the thermal X-ray emission from the hot neutron star’s surface should be unchanged from 2000 to 2012. The analysis of the spectrum and flux of this source by Heinke et al. (2014), which compared the two *Chandra* epochs and the *XMM-Newton* epoch, shows no detectable variation, consistent with this picture.

4 X-RAY SOURCE MEMBERSHIP

Given the length of the ACIS-I exposures and the sensitivity of the camera, significant numbers of AGN will be present in the data, as well as foreground stars. The cumulative number of sources as a function of flux in the entire 2012 field of view (FOV) is shown in Fig. 4, together with results obtained by Luo et al. (2008) for the *Chandra* Deep Field South (CDF-S).⁴ These authors analysed a ~ 2 Ms exposure of the CDF-S, detecting 578 sources in a ~ 436 square arcminute field of view with limiting sensitivity of $f_X \approx 1.9 \times 10^{-17}$ ergs cm $^{-2}$ s $^{-1}$ in the 0.5–2.0 keV band. Scaling the CDF-S results to the ~ 286 square arcminute field of view of the present study reveals a clear excess of sources toward ω Cen with fluxes in excess of $f_X(0.5\text{--}2.0 \text{ keV}) \sim 2 \times 10^{-16}$ erg s $^{-1}$ cm $^{-2}$ (see Fig. 4). At $f_X(0.5\text{--}2.0 \text{ keV}) = 5 \times 10^{-15}$ erg s $^{-1}$ cm $^{-2}$, for example, the cumulative excess is a factor of two, with 29 sources observed and only ~ 14 AGN predicted. At $f_X(0.5\text{--}2.0 \text{ keV}) = 5 \times 10^{-16}$ erg

⁴ A table of values corresponding to the 2 Ms CDF-S measurements, corrected for incompleteness as shown in Fig. 15a of Luo et al. (2008), was kindly provided by B. Luo.

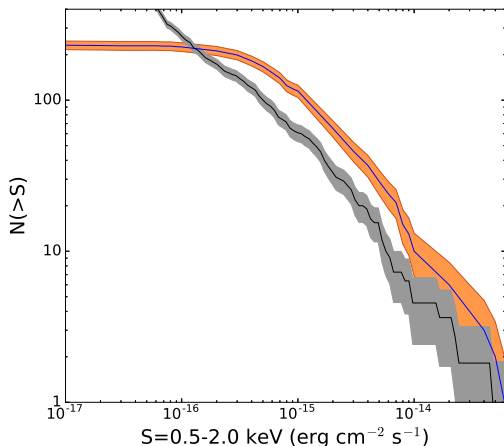


Figure 4. The number of sources N that are brighter than a given flux S in the CDF-S 0.5–2.0 keV energy band (blue line with \sqrt{N} error range in red). The predicted number of AGN based on the *Chandra* Deep Field South study of Luo et al. (2008) is shown as a black line with \sqrt{N} error range in grey.

$\text{s}^{-1} \text{cm}^{-2}$, the cumulative excess is still ~ 70 per cent, with 169 sources observed and only ~ 100 AGN predicted.

To examine the radial dependence of the X-ray source distribution in ω Cen we have divided the ACIS-I field of view into four regions: the cluster core, two concentric annuli ($1-2r_c$, $2-3r_c$), and a fourth region that includes all ACIS-I area outside $3r_c$ (see Fig. 5). The first three regions are fully encompassed within the ACIS-I field of view and occupy approximately 21, 63, and 105 square arcminutes, respectively, while the fourth spans the remaining ~ 97 square arcminutes. Dividing up the field in this way enables us to take the radial dependence of the limiting flux into account. The cumulative number of sources as a function of flux in the 0.5–2.0 keV CDF-S soft band are shown as solid blue lines in Fig. 5. The predicted numbers of AGN (Luo et al. 2008), scaled to the area of each region, are shown for comparison (dashed black lines) with dotted black lines representing root N uncertainties. The difference, i.e. sources not attributable to background AGN, are shown as solid red lines.

These plots confirm that significant numbers of X-ray sources toward ω Cen cannot be attributed to background AGN, and that this is true not only in the core of the cluster, but also in the $1-2r_c$ annulus. Specifically, we estimate that 33 ± 4 and 33 ± 6 sources in these two regions, respectively, cannot be attributed to AGN.⁵ In the outer two regions, the numbers are smaller but still non-negligible, with 14 ± 5 , and 12 ± 5 sources unattributed to AGN in the $2-3r_c$ and $> 3r_c$ regions, respectively. The total number of sources unattributed to AGN is thus $\sim 90 \pm 20$. These numbers increase by ~ 15 sources if, like Haggard et al. (2009), we derive AGN estimates from Tozzi et al. (2001) rather than Luo et al. (2008).

Estimating how many of the sources may be foreground stars is more challenging given the variations in star counts as a function of Galactic latitude and longitude. A rough idea can be gleaned from the *XMM-Newton* SSC survey of the galactic plane (Nebot Gómez-Morán et al. 2013), which combines results

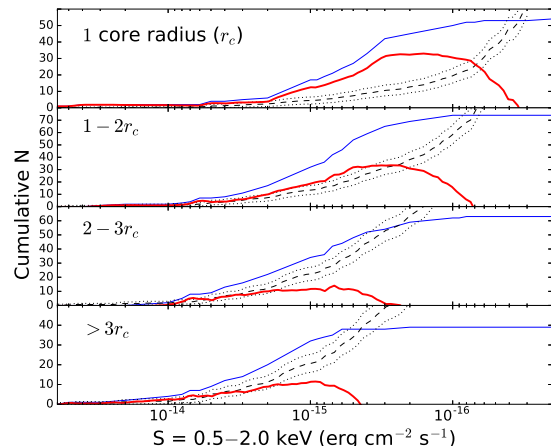


Figure 5. Cumulative numbers of observed sources in four regions as a function of flux in the 0.5–2.0 keV band (solid blue lines). Expected numbers of background sources scaling from Luo et al. (2008) are given as dashed black lines with uncertainties presented as dotted black lines. The resultant numbers of sources not attributable to background AGN are shown as solid red lines.

for fields with galactic latitudes in the range $b = 12-19^\circ$ and longitudes in the range $l = 54-237^\circ$. For comparison, ω Cen has $b = 15^\circ$ and $l = 51^\circ$. Extrapolating the Nebot Gómez-Morán et al. (2013) results for known and suspected coronal sources at $|b| = 15^\circ$ (see red dotted line in their Fig. 16) from their $f_X(0.5-2.0 \text{ keV})$ limit of $\sim 3.4 \times 10^{-15} \text{ erg s}^{-1} \text{cm}^{-2}$ to the f_X values at the peaks of the four red curves in Fig. 5 suggests that perhaps 30–40 of the sources could be stars with active coronae ($\sim 6, 12, 10$, and 8 in the four radial regions, respectively). This leaves an estimated $\sim 54 \pm 20$ sources associated with ω Cen. This is likely to be a lower limit, considering that the extrapolation is being made to fluxes that are as much as a factor of 10 fainter than those sampled by Nebot Gómez-Morán et al. (2013) and will tend to overestimate the number of coronal sources in the foreground since the line of sight to ω Cen extends outside of the thin disc where most foreground sources should lie.

For another perspective on source membership, we plot X-ray flux in the CDF-S band as a function of the square of the offset from the cluster centre in Fig. 6. Here it can be seen that the density of sources appears highest close to the cluster centre, dropping off with increasing radius, whereas background and foreground sources should spread evenly across the plot. To investigate how the radial distribution depends on flux, we adopt four flux bins (see dotted lines in Fig. 6). Three of the sources in the brightest bin [$f_X(0.5-2.0 \text{ keV}) > 3 \times 10^{-14} \text{ erg s}^{-1} \text{cm}^{-2}$], which corresponds to $L_X \gtrsim 10^{32} \text{ erg s}^{-1}$ at a distance of 5.2 kpc, are already known to be cluster members (CVs 13a and 13c, and qLMXB 44e; Carson et al. 2000; Haggard et al. 2004). The fourth we propose is a CH star that is also a cluster member (see Section 6).

The next bin, $f_X(0.5-2.0 \text{ keV}) = 3-30 \times 10^{-15} \text{ erg s}^{-1} \text{cm}^{-2}$ ($L_X \gtrsim 10^{31}-10^{32} \text{ erg s}^{-1}$), contains 42 sources: 3, 11, 14, and 14 in the four radial bins, respectively. In this flux range, the census of sources should be complete out to nearly the edge of the field (see Fig. 6). There is no measurable excess of sources toward the cluster centre; the relative numbers of sources in the four bins scale roughly with the relative areas of the bins. However, the predicted number of AGN (Luo et al. 2008) and foreground stars (Nebot Gómez-Morán et al. 2013) in the ACIS-I FOV in this flux

⁵ Taking account of the reduced sensitivity in chip gaps reduces the predicted numbers of AGN in the core by 1–2 sources, and correspondingly increases the estimated number of member sources. Outside the core the correction is negligible.

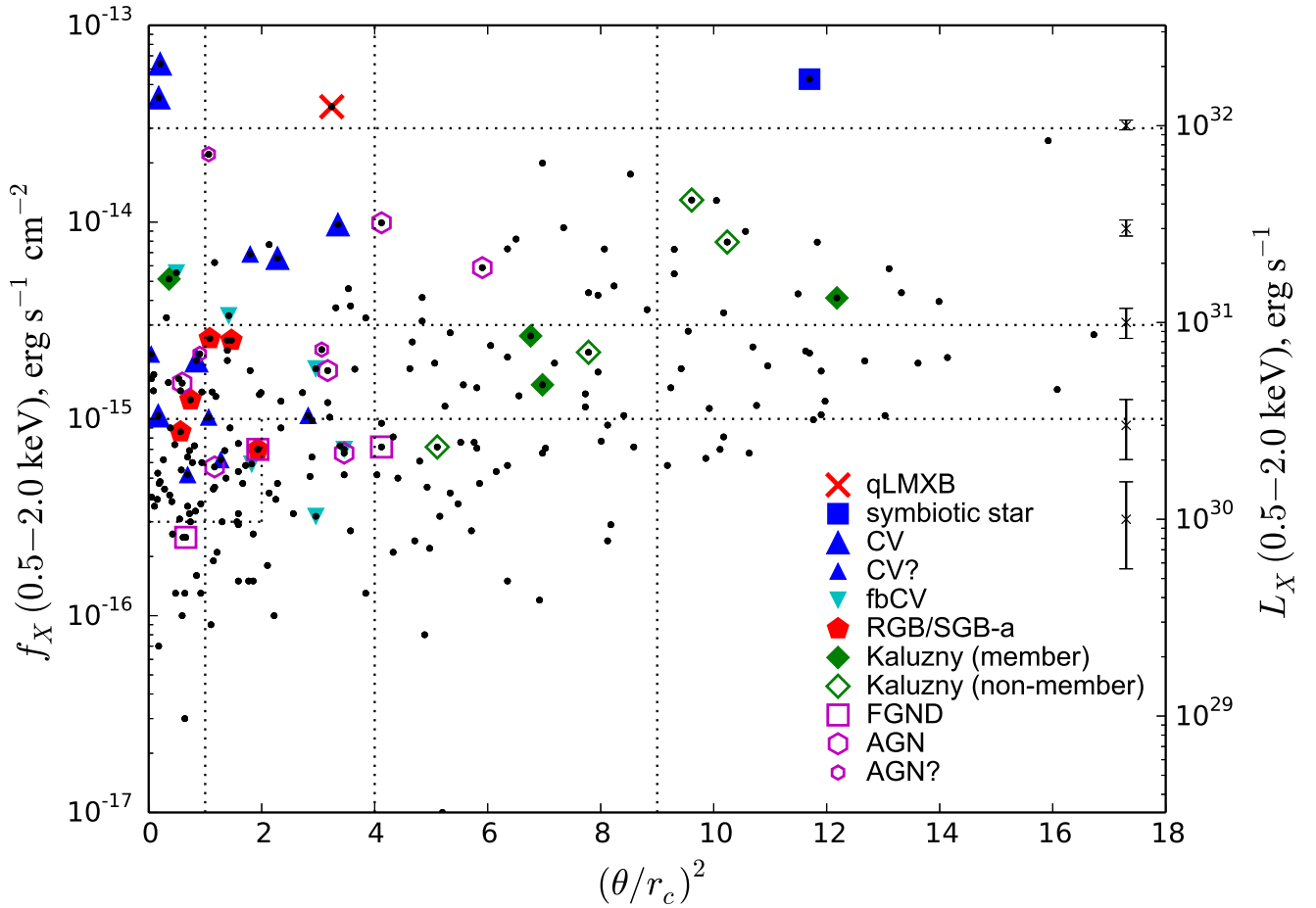


Figure 6. Flux in the CDF-S 0.5–2.0 keV band as a function of the square of the radial offset from the cluster centre in units of the core radius ($r_c = 155$ arcsec). Solid coloured symbols mark sources for which reported optical IDs (see Figs. 5–7 in [Cool et al. \(2013\)](#)) are probable cluster members; open symbols mark sources which are outside the cluster (based on their optical IDs). Kaluzny designation refers to variable stars identified by [Kaluzny et al. \(1996, 2004\)](#). Representative error bars are shown at right. Dotted lines demarcate regions used to analyse the radial distribution of sources as a function of flux (see Section 4).

range are 22 ± 5 and 7 ± 3 , respectively, which suggests that $\sim 13 \pm 8$ of the sources are associated with the cluster. That at least some are probable cluster members is corroborated by optical IDs whose characteristics suggest membership (see solid coloured symbols in Fig. 6).

A noticeable central concentration of sources is apparent for fainter sources with fluxes in the bin of range $f_X = 1\text{--}3 \times 10^{-15}$ erg s $^{-1}$ cm $^{-2}$, or $L_X \sim 3 \times 10^{30} \text{--} 1 \times 10^{31}$ erg s $^{-1}$ (see Fig. 6). In this bin, source counts are clearly incomplete in the outermost radial bin, but should be reasonably complete inside $3r_c$. A total of 51 sources are present inside $3r_c$ in this flux range: 13 in the core, 20 in the $1\text{--}2r_c$ annulus, and 18 in the $2\text{--}3r_c$ annulus. Scaling from [Luo et al. \(2008\)](#), ~ 3 , ~ 8 , and ~ 14 AGN are expected in these three regions, respectively. Scaling from [Nebot Gómez-Morán et al. \(2013\)](#), another ~ 1 , ~ 2 , and ~ 4 sources are likely to be foreground stars. While these numbers are small and subject to considerable uncertainties, they suggest that AGN and foreground stars could account for all or most of the sources in the $2\text{--}3r_c$ annulus. In the core and first annulus ($1\text{--}2r_c$), however, there is an excess of ~ 9 and ~ 10 sources, respectively. Similar results are obtained if we simply

use the sources in the $2\text{--}3r_c$ annulus as a measure of the surface density of non-members in this flux range. Thus we estimate that ω Cen contains a total of ~ 20 X-ray sources with luminosities in the range $L_X \sim 3 \times 10^{30} \text{--} 1 \times 10^{31}$ erg s $^{-1}$, and that these are roughly evenly split between the core and the $1\text{--}2r_c$ annulus.

For fluxes below $f_X = 10^{-15}$ erg s $^{-1}$ cm $^{-2}$ ($L_X \lesssim 3 \times 10^{30}$ erg s $^{-1}$), source counts begin to show signs of incompleteness even in the outer part of the $1\text{--}2r_c$ radial bin. Still, a comparison of the number of sources in the core with fluxes in the range $f_X = 3 \times 10^{-16} \text{--} 1 \times 10^{-15}$ erg s $^{-1}$ cm $^{-2}$ to the number in an annulus of the same surface area immediately outside the core (26 and 17, respectively; see dotted regions in Fig. 6) reveals an excess in the core. [Luo et al. \(2008\)](#) predict only ~ 6 AGN in a region the size of the core in this flux range, and scaling from [Nebot Gómez-Morán et al. \(2013\)](#) predicts ~ 2 foreground coronal sources. Thus the core of ω Cen contains $\sim 15\text{--}20$ X-ray sources with $L_X \approx 1\text{--}3 \times 10^{30}$ erg s $^{-1}$, and perhaps 10–15 of the ~ 30 sources in the $1\text{--}2r_c$ annulus are also cluster members.

In summary, this flux-based analysis reveals a total of $\sim 67 \pm 20$ cluster members, consistent with the range of 54 ± 20 derived from

the Fig. 5 plots. This is likely to be a lower limit on the actual number of X-ray sources in ω Cen since the number of member sources appears to increase steadily as the limiting flux is approached and we have not counted sources in radial/flux bins in which incompleteness is significant.

5 OPTICAL IDENTIFICATIONS

While it is clear that ω Cen is host to a large number of X-ray sources, optical IDs are required to determine which ones are cluster members and what they are. The most interesting new identification presented here is a CH star that coincides with the second brightest source in the ACIS-I field, 94a. We suggest that it is a symbiotic star – the first such star discovered in a globular cluster – and discuss it further below (see Section 6).

Identifications of previously known sources given by Haggard et al. (2009) and Cool et al. (2013, see their Figs. 5–7) are listed in column 13 of Table 3.⁶ These include compact binaries (CVs and a qLMXB), AGN, foreground stars, and variable stars both in and out of the cluster. Subsets of these classes whose identities are uncertain are listed with ‘?’ following the ID. We also include several stars identified by Cool et al. (2013) as possible members of ω Cen’s anomalously metal-rich red-giant and/or subgiant branches (RGB/SGB-a).⁷

We searched the variable star catalogue of Kaluzny et al. (2004) for matches to any of the 233 Cycle 13 sources. We found three new matches: 63h = NV410, 73a = NV369, and 91a = NV379. All are variables of unknown type with variability periods of 1.8, 7.1, and 14.5 days, respectively. These are listed in column 13 of Table 3 along with five previously known matches (Haggard et al. 2009). These new potential matches have offsets between the optical and X-ray positions of 1.19 arcsec, 1.46 arcsec, and 1.20 arcsec, respectively.⁸

The offsets between these possible new IDs and the X-ray positions place them somewhat outside the 95 per cent error circles (see Table 3) computed following the empirical prescription of Hong et al. (2005) – by factors of 1.14, 1.97, and 1.04, respectively. However, in view of the large off-axis angles involved (and larger uncertainties associated with centroiding the X-ray counts given the broad PSF), combined with the potential for additional uncertainties associated with the Kaluzny positions and/or proper motions of non-members, we chose to consider matches to within 1.5 arcsec as potentially real. No other matches of Kaluzny et al. (2004) variable stars to new *Chandra* sources were found with offsets under 2.0 arcsec.

To determine the rate of chance coincidences resulting from our choice of 1.5 arcsec error circles, we increased the error circle radii to 15 arcsec and reran the search. This resulted in one or more Kaluzny variables landing in 56 of the 233 expanded error circles, implying an average expected rate of 0.56 chance coincidences with the error circles actually in use. Applying Poisson statistics, we find that it is more likely than not that all eight Kaluzny IDs reported here are real. However we cannot rule out the possibility that one

or two could be chance alignments (Poisson probability 32 per cent and 9 per cent, respectively).

We also searched for matches of *Chandra* sources with the catalogues of Weldrake et al. (2007) and Lebzelter & Wood (2016) and to the Henry Draper (HD) catalogue and found no other counterparts. Work to identify additional optical counterparts using *HST* data is underway and will be reported elsewhere.

For some optical IDs (e.g. AGN), membership status is clear from their very nature. For others (e.g. CVs), a concentration toward the cluster centre indicates that most if not all are associated with the cluster. In other situations cluster membership is more difficult to assess, and in these cases proper motions are invaluable. Bellini et al. (2009) have measured proper motions for more than 300 of the 9 such IDs reported here (see Table 3). Three of these (NV369=73a, V216=74d, and NV379=91a) have membership probabilities in the range 94–99 per cent and are thus very likely members. A fourth, NV371=11b, has a membership probability of 100 per cent according to van Leeuwen et al. (2000). Of the other four, according to Bellini et al. (2009), two (NV377=82b and NV410=63h) are clear non-members (membership probability = 0 per cent), and two others are probably unassociated with the cluster (membership probabilities are 15 per cent and 23 per cent for V210=73d and V167=84d, respectively). Optical counterparts that are unlikely to be associated with ω Cen are shown in parentheses in column 13 of Table 3.

6 A SYMBIOTIC STAR IN OMEGA CENTAURI

The second-brightest source in the ACIS-I field of view (94a) lies about 8.8 arcmin southwest of the cluster centre (see Figs. 1 and 2) with a flux of $f_X(0.5\text{--}4.5\text{ keV}) = 1.0 \times 10^{-13}\text{ erg s}^{-1}\text{ cm}^{-2}$. This source was also detected in our first epoch of *Chandra* data (Haggard et al. 2009), with *XMM-Newton* (Gendre et al. 2003, their source #1) and with *ROSAT/PSPC* (Johnston et al. 1994, their source #11), but has not previously been identified optically. In the *XMM-Newton* study it was the brightest and hardest source, and was variable on time-scales of minutes to hours (Gendre et al. 2003, see their Fig. 6).

The position of this source coincides closely with a Population II carbon star that was identified by Harding (1962, star 0055) – the first CH star to have been found in a globular cluster. The star, which lies near the tip of the RGB at $V = 11.49$ and $B-V = 1.74$ (Harding 1962), was later catalogued by van Leeuwen et al. (2000) as CI NGC 5139 LEID 52030 at R.A. = $13^h26^m01^s.61$, Dec. = $-47^\circ33'05''.7$. This is 0.34 arcsec from the *Chandra* position for source 94a, inside the 95 per cent confidence radius of 0.55 arcsec (see Table 3). The star was shown to be a radial-velocity member of the cluster by Mayor et al. (1997) and a proper-motion member at 99 per cent confidence by van Leeuwen et al. (2000). It has since been included in studies of mass-loss and dust production among giants in ω Cen (van Loon et al. 2007; McDonald et al. 2009).

We propose that this object is a symbiotic star in ω Cen. CH stars in the field are known to have compact binary companions that are typically white dwarfs McClure (1984); McClure & Woodsworth (1990). If the WD is accreting from the giant’s wind then it will appear as a symbiotic star (Kenyon 1986). We show in Section 7 that its X-ray properties are similar to several symbiotic stars recently observed with Suzaku (Nuñez et al. 2016). Details concerning this star will appear in a forthcoming paper.

⁶ Those designated ‘blue-only’ or ‘H α -only’ in Cool et al. (2013) are least secure and are excluded here, along with the apparent blue straggler counterpart to 22d which has since been shown to be a non-member by Deveny et al. (2016).

⁷ One object (13b) which does not lie on this branch but was previously included in this category is excluded here.

⁸ Including a boresight correction does not change these values significantly.

7 X-RAY CMD AND BRIGHT-SOURCE ANALYSIS

Further clues to the nature of the X-ray sources in ω Cen can be gleaned from an examination of the cluster's X-ray colour-magnitude diagram (CMD) shown in Fig. 7a. Here we plot the wide-band (0.5–6.0 keV) flux vs. X-ray colour ($X_{\text{colour}} = 2.5 \times \log[X_{\text{soft}}/X_{\text{hard}}]$); the corresponding L_X is indicated on the left-hand side assuming a distance of 5.2 kpc. Objects with known or suggested optical counterparts are indicated with coloured symbols. Solid and open symbols signify cluster members and non-members, respectively. For comparison, we also plot hardness ratios for several spectral models, using the known cluster absorption unless otherwise indicated. Thermal plasma models (vmekeal in XSPEC) appear at the top and power-law models appear at the bottom; the vertical position is arbitrary. The effect of increasing the hydrogen column is indicated for several values of n_H for a 10 keV thermal plasma spectrum. Finally, hydrogen atmosphere neutron star models are plotted for a range of temperatures, assuming a 10 km radius. In Fig. 7b we show the same diagram, but with symbols indicating location relative to the cluster centre. Errors on a subset of the points are also shown to illustrate how the uncertainties depend on location within the plot.

The three brightest X-ray sources – two CVs and the CH star – all have hard X-ray colours suggestive of internal absorption. The fainter CVs and CV candidates display a significantly larger spread in colours and are softer on average than the brightest CVs. The known AGN have X-ray colours similar to the CVs, highlighting the importance of optical identifications. The X-ray sources associated with variable stars from Kaluzny et al. (1996, 2004) have relatively soft X-ray colours, similar to those of the three known foreground stars, consistent with their probable coronal nature. X-ray colours of the RGB/SGB-a stars are intermediate between the accretion sources and the coronal sources.

For further insight into the brightest cluster X-ray sources, we performed spectral fitting for 14 sources whose optical counterparts suggest they are cluster members. We selected sources with at least 70 counts in the 0.5–6.0 keV band. This includes the CH star, nine CVs and CV candidates, two stars that lie on the anomalous RGB/SGB, and two of the Kaluzny variables. Since the spectrum of the qLMXB has already been reported elsewhere (Heinke et al. 2014, see also Rutledge et al. (2002)), we do not discuss it here.

We began by combining the spectra from the two Cycle 13 ObsIDs using the HEASoft tool ADDSPEC. We then fitted the combined spectra using HEASoft/Xspec and C-statistics (Cash 1979). We fit vmekeal models (tbabs*vmekeal), specifying abundances appropriate for the dominant $[\text{Fe}/\text{H}] = -1.5$ stellar population in ω Cen. For the faintest sources we fixed the column at the cluster value of $n_H = 9 \times 10^{20} \text{ cm}^{-2}$, while for those with at least 100 counts we allowed the n_H value to vary, which yields a more meaningful constraint on kT. Best-fitting parameters, including 90 per cent confidence intervals, are reported in Table 2.

For the CH star and five of the nine brightest CVs and CV candidates no satisfactory fit could be obtained at the cluster n_H value, corroborating the X-ray CMD results. For these sources (94a, 13c, 13a, 54h, 41d, and 54b), the cluster n_H value is excluded at 90 per cent confidence or more. The required n_H values for these sources lie in the range $4 \times 10^{21} - 2 \times 10^{22} \text{ cm}^{-2}$, similar to what Heinke et al. (2005) found for the most strongly absorbed sources in 47 Tuc. Internal absorption was also required to obtain a good fit for source 34b, an RGB/SGB-a star. We discuss the significance of these findings below (see Section 8). For four other sources for which n_H was allowed to vary (43h, 22c, 31a, and 11b), no internal

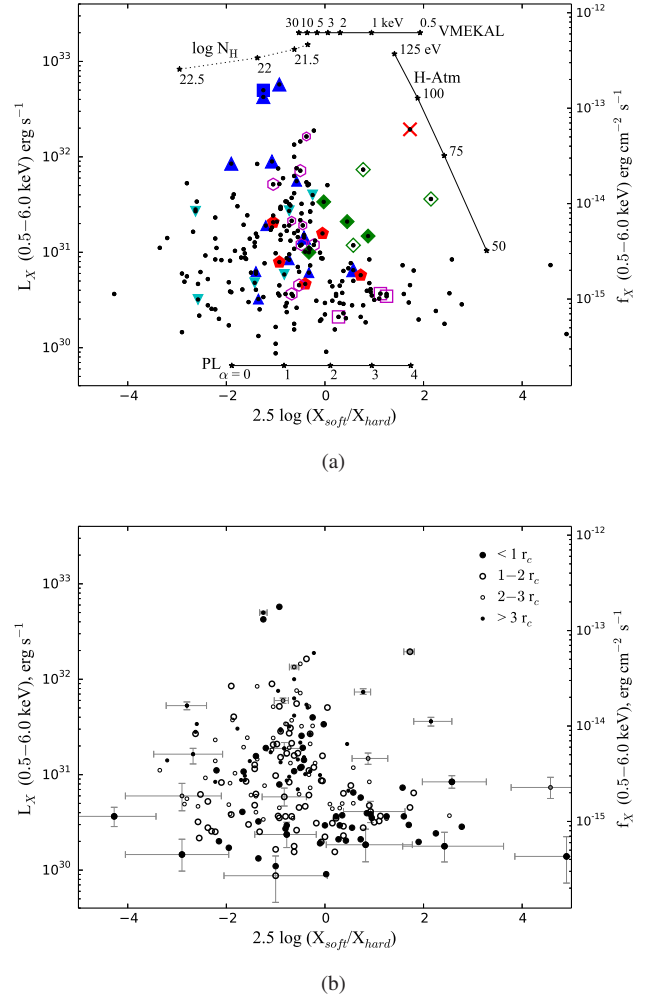


Figure 7. (a) An X-ray ‘colour-magnitude’ diagram for 221 *Chandra* sources that have non-zero fluxes in both the hard (1.5 – 6.0 keV) and soft (0.5 – 1.5 keV) bands. Symbols as in Fig. 6. Hardness ratios for several spectral models are shown using the known cluster absorption. Thermal plasma models (vmekeal in XSPEC) are shown near the top of the figure; power-law models appear close to the bottom (vertical position is arbitrary). The effect of increasing the hydrogen column is indicated for several values of n_H for a 10 keV thermal plasma spectrum. Hydrogen atmosphere neutron star models are plotted for a range of temperatures assuming a 10 km radius. (b) Same as top panel, but with symbols indicating location of sources in the cluster. Confidence intervals (68 per cent) on the X-ray colour values and wide-band fluxes calculated using the Bayesian estimation method outlined in Park et al. (2006) are shown for a representative sample of sources.

absorption was required to obtain a satisfactory fit. All the CVs and CV candidates were well fit with plasma temperatures in the range 6–30 keV which is typical of CVs (Mukai 2017). The CH star, with a plasma temperature of 7 keV, appears softer than the two CVs with comparable luminosities. Its temperature, luminosity, and enhanced n_H values are all within the range of properties deduced for a set of symbiotic stars observed with Suzaku (Nuñez et al. 2016). The two RGB/SGB-a stars and one of the Kaluzny variables have lower plasma temperatures in the range 2–3 keV which is more typical of coronal sources (Dempsey et al. 1993, 1997). Sample spectra are shown in Fig. 8.

We also searched the X-ray lightcurves of these 14 bright

Table 2. Spectral Fits of Brightest Sources in Omega Cen.

Source	Type	Counts (0.5–6.0 keV)	n_H [†] (10^{20} cm ⁻²)	kT (keV)	$L_{X,abs}$ [‡] (10^{30} erg s ⁻¹)	$L_{X,unabs}$ [‡] (10^{30} erg s ⁻¹)
94a	CH star	1092	72^{+16}_{-15}	$6.8^{+3.3}_{-1.7}$	466^{+25}_{-26}	662^{+52}_{-52}
13c	CV	2252	16^{+6}_{-6}	$34.0^{+45.4}_{-13.9}$	570^{+21}_{-21}	627^{+27}_{-27}
13a	CV	2053	51^{+8}_{-8}	$14.4^{+7.9}_{-4.0}$	423^{+16}_{-16}	539^{+27}_{-27}
54h	CV	440	37^{+20}_{-18}	$19.2^{+\infty}_{-10.5}$	98^{+8}_{-8}	119^{+9}_{-10}
41d	CV	407	112^{+35}_{-30}	$14.6^{+\infty}_{-7.7}$	117^{+9}_{-10}	172^{+14}_{-14}
43h	CV?	224	12^{+16}_{-3*}	$6.8^{+8.2}_{-3.1}$	49^{+5}_{-5}	54^{+6}_{-6}
22c	fbCV?	193	11^{+15}_{-2*}	$5.7^{+5.6}_{-2.1}$	35^{+4}_{-4}	39^{+4}_{-5}
31a	fbCV?	130	21^{+25}_{-12*}	$22.3^{+57.6}_{-15.7}$	27^{+4}_{-4}	31^{+4}_{-4}
54b	fbCV?	125	196^{+84}_{-72}	$13.0^{+\infty}_{-8.3}$	34^{+5}_{-5}	58^{+8}_{-9}
24c	CV	75	(9)	$5.7^{+13.2}_{-2.7}$	12^{+2}_{-2}	13^{+2}_{-3}
34b	RGB/SGB-a	93	55^{+41}_{-34}	$2.7^{+4.4}_{-1.0}$	17^{+3}_{-3}	25^{+4}_{-4}
32f	RGB/SGB-a	76	(9)	$2.2^{+1.6}_{-0.7}$	12^{+2}_{-2}	13^{+2}_{-3}
11b	NV371	177	9^{+7}_{-0*}	$3.2^{+1.2}_{-0.7}$	26^{+3}_{-3}	29^{+3}_{-4}
73a	NV369	71	(9)	$8.8^{+47.6}_{-5.1}$	18^{+3}_{-4}	19^{+4}_{-4}

Note. — [†]Parentheses indicate that the parameter was frozen during the fit; [‡]Luminosities are given in the 0.5 – 6.0 keV band; *Lower limits are below minimum limiting value for n_H (9×10^{20} cm⁻²).

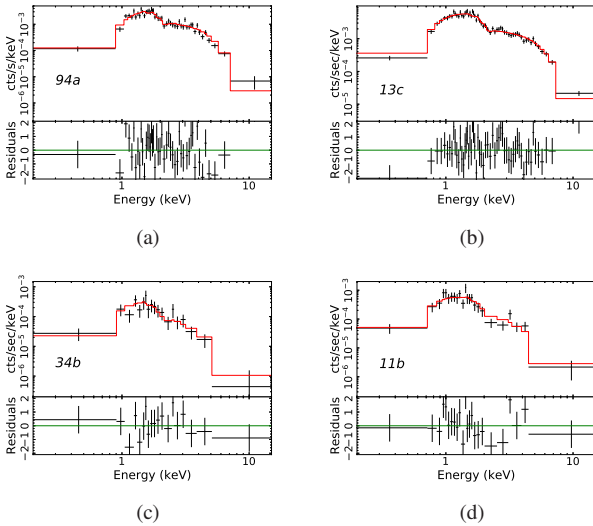


Figure 8. Spectra of four X-ray sources in ω Cen: (a) the CH star (94a), (b) the brightest CV (13c), (c) the brightest RGB/SGB-a star (34b), and (d) the brightest of the Kaluzny variables (11b). Solid red lines in upper panels represent fits of *vmekal* models to the Cycle 13 spectra made using a maximum-likelihood procedure (see text). Spectra are binned for plotting purposes only. Lower panels show the residuals: (data–model)/error.

sources for signs of variability. We used CIAO’s *GLVARY* tool to search for variability within each Cycle 13 ObsID. The CIAO *GLVARY* tool applies the Gregory-Loredo variability algorithm (Gregory & Loredo 1992) which looks for significant changes between events in different time bins, and assigns a variability index and a probability that the flux from the source region is time-variable. We also searched for variations between the two ObsIDs by simultaneously fitting spectra extracted from each while allowing the normalization to differ. The CH star shows clear variability in the longer of the two ObsIDs (*GLVARY* index = 6), with evident flaring activity (see Fig. 9). Several other sources show hints of variability up to ~ 50 per cent, but none with greater than 90 per cent confidence. Additional spectral and variability analyses are underway and will be presented elsewhere.

Among the sources in the X-ray CMD that have yet to be identified optically, many have rather hard X-ray colours (e.g. requiring more than 3×10^{21} cm⁻² of additional absorption). This is unlikely to be the result of differential interstellar absorption, which should be relatively small across our field (of order 10 per cent; Bellini et al. 2017). However it is not unexpected given that the majority of the unidentified sources are likely to be AGN (see Section 4), which have hard spectra and frequently show internal absorption (Hasinger et al. 2001; Kim et al. 2004). Of the 45 sources with optical IDs thus far, 29 appear to be members, leaving ~ 30 member sources yet to be identified out of more than 180 with no IDs at present.

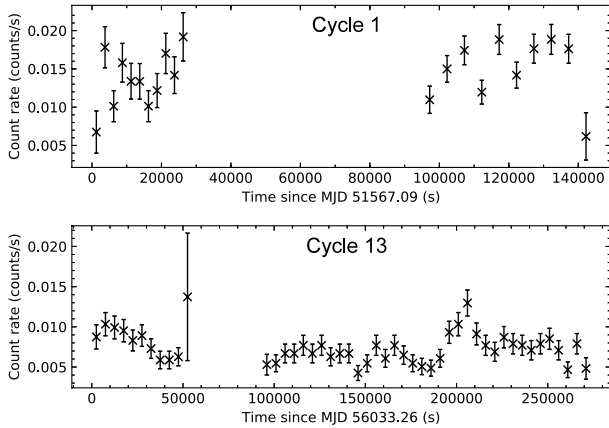


Figure 9. X-ray lightcurve for source 94a, a proposed symbiotic star in ω Cen. Cycle 1 and Cycle 13 data are shown in top and bottom plots, respectively, each of which are divided into two separate observation periods (ObsIDs). Significant flaring activity can be seen in the second Cycle 13 ObsID.

8 DISCUSSION

These *Chandra* observations bring the total number of X-ray sources known in and toward Omega Centauri to 275, a factor of ~ 1.5 increase over those previously known (Haggard et al. 2009). Of the 233 sources in the present data, we estimate that $\sim 60 \pm 20$ are associated with the cluster. The remainder are primarily AGN, with a smaller contribution from foreground stars. In projection, approximately 30 of the cluster sources reside in the core; a similar number lie in a $1-2r_c$ annulus surrounding the core. The sources range in luminosity from $L_x \sim 1 \times 10^{30}$ to 6×10^{32} erg s $^{-1}$ in the 0.5–6.0 keV band, or $\sim 3 \times 10^{29}$ to 2×10^{32} erg s $^{-1}$ in the 0.5–2.0 keV band. Relatively few member sources lie outside $2r_c$, but our knowledge of this population is more limited owing to the drop in sensitivity off-axis. In the 0.5–2.0 keV band, these observations should be complete to $L_x \approx 10^{30}$ erg s $^{-1}$ in the cluster core and to $L_x \approx 10^{31}$ erg s $^{-1}$ over the full ACIS-I field of view (see Fig. 6).⁹

Optical identifications reported in previous studies, combined with four new IDs presented here, bring the number of X-ray sources in ω Cen with secure or promising optical counterparts to 45. These include 29 cluster members, 20 of which are accretion-powered: one qLMXB, 18 CVs and CV candidates, and one newly identified symbiotic star. Nine others are most likely coronal sources: five stars that lie along ω Cen’s anomalous giant and subgiant branch and four variable stars.

Cataclysmic variables dominate the X-ray source population in ω Cen for which optical IDs exist. Extrapolating their fraction (18/29) to the total X-ray source population suggests a total of $\sim 40 \pm 10$ CVs in ω Cen with $L_x(0.5-2.0 \text{ keV}) \geq 10^{30}$ erg s $^{-1}$, compatible with the upper end of an earlier estimate made by Haggard et al. (2009). Given the greater ease with which accretion vs. coronal sources can typically be identified in optical searches, this may be an overestimate. Still, it seems probable that at least ~ 30 CVs are present in ω Cen given the number already known, the difficulty of obtaining optical identifications in crowded fields like ω Cen, and

the fact that optical follow-up has yet to be undertaken for the 95 newly-identified X-ray sources.

Theoretical work shows that CVs in globular clusters should form through two distinct channels. Primordial binaries that would have given rise to CVs in the field can, under favourable conditions, similarly produce CVs in a GC (Davies 1997; Ivanova et al. 2006). Dynamical interactions taking place primarily in cluster cores provide a second channel. The dominant mechanism for CV formation in this case involves an exchange interaction in which a typically heavy white dwarf is exchanged into a primordial binary consisting of two main-sequence stars. This channel is favoured in clusters with high-density and/or large cores which generate high rates of stellar interactions (Ivanova et al. 2006; Belloni et al. 2016; Hong et al. 2017).

Omega Cen presents an interesting case in the context of these two CV formation channels. Given the sheer number of stars it contains, it is likely to have formed with many of the primordial binaries that could give rise to CVs, and its modest central density ($\rho_0 \sim 3 \times 10^3 \text{ M}_\odot/\text{pc}^3$; Pryor & Meylan 1993) favours the survival of such systems. At the same time, because it has a very large core ($r_c \approx 3.9 \text{ pc}$), the overall rate of stellar interactions is high enough that CVs are also expected to form via dynamical interactions (Verbunt & Meylan 1988; Davies & Benz 1995). In addition, ω Cen’s half-mass relaxation time is sufficiently long (1.2×10^{10} yr; Harris 2010) that, in contrast to most GCs with significant rates of stellar interactions, ω Cen is far from being relaxed, as demonstrated by its lack of significant mass segregation (Anderson 2002). This further favours the survival of primordial binaries that could give rise to CVs, since they are less likely to have sunk to the more perilous central regions of the cluster despite their larger-than-average masses. Moreover, in contrast to CVs in most other GCs whose radial distribution reflects their masses (e.g. Cohn et al. 2010), the distribution of CVs in ω Cen should be more indicative of where they formed, regardless of origin.

The radial distribution of optically identified CVs in ω Cen can be seen in Fig. 10, in which we plot X-ray luminosity as a function of radius in the cluster.¹⁰ More than half of the known CVs lie outside $0.5r_h$; there is no sign that CVs preferentially reside in the denser central region of the cluster. This is in contrast to other clusters in which significant numbers of CVs have been observed. In NGC 6397, NGC 6752, and 47 Tuc, CVs are clearly concentrated toward the cluster centres and dynamical interactions appear to be implicated in the formation of at least some of these systems (Cohn et al. 2010; Lugger et al. 2017; Rivera-Sandoval et al. 2018). The markedly different radial distribution observed here suggests that the bulk of the CVs in ω Cen have their origins as primordial binaries, which have survived by inhabiting the regions outside the cluster core.

While it appears likely that ω Cen’s CV population is dominated by systems originating from primordial binaries, it is interesting to ask if there are indications that any of the CVs in the cluster could be of dynamical origin. The rate of stellar interactions in ω Cen is expected to be comparable to the collapsed-core cluster NGC 6397 (Bahramian et al. 2013) whose central density is ~ 60 times higher than ω Cen’s (Pryor & Meylan 1993), but whose core is far smaller. Among the 15 CVs in NGC 6397, several appear to be of dynamical origin: their concentration toward the cluster cen-

⁹ These L_x values increase by a factor of $\sim 2-3$ if we consider the 0.5–6.0 keV band instead.

¹⁰ *HST*-based searches for optical counterparts to date have focused on the region interior to r_h (Cool et al. 2013); less is known about CVs outside the half-mass radius.

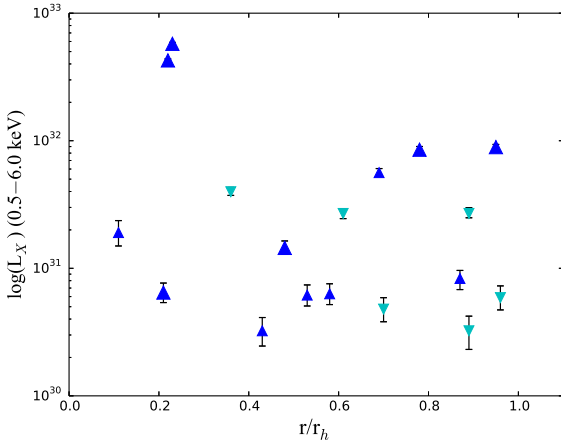


Figure 10. X-ray luminosity of CVs and CV candidates as a function of radius in ω Cen, in units of the half-mass radius (5.0 arcmin). Symbols as in Fig. 6.

tre implies high masses that are likely the result of exchange collisions, and their high luminosities are indicative of youth (Cohn et al. 2010). Of these, the four most luminous CVs, with $L_X(0.5\text{--}6.0\text{ keV}) > 5 \times 10^{31}\text{ erg s}^{-1}$ lie in or very near the cluster core. In ω Cen, the two most luminous CVs lie well inside the core ($r_c = 2.6$ arcmin), just 1.1 arcmin and 1.2 arcmin from the cluster centre, respectively. While the numbers are small, this is at least a hint that the dynamical formation channel is operating in ω Cen. The probability that the two most recently formed primordial CVs would both lie so close to the cluster centre by chance is ~ 1 per cent judging from the number of stars inside 1.2 arcmin vs. inside $2r_c$.¹¹ Moreover, the rate of interactions involving heavy remnants may be highest in the inner region of the core where these sources lie. Given ω Cen’s ~ 4 Gyr central relaxation time, such remnants, which are more massive than average stars in the core and formed early in the cluster’s history, would have had time to form a relaxed and thus more centrally concentrated distribution than the main-sequence stars in the core.

While ω Cen harbours a substantial population of CVs, their numbers appear low by comparison to the field. Based on a sample of 20 non-magnetic CVs with $L_X(0.5\text{--}2.5\text{ keV}) \sim 10^{30}\text{--}10^{32}\text{ erg s}^{-1}$, Pretorius & Knigge (2012) deduce a CV space density of $4^{+6}_{-2} \times 10^{-6}\text{ pc}^{-3}$ (1 σ confidence interval) in the solar neighborhood. The range of X-ray luminosities we sample in ω Cen is very similar. The estimated population of 40 ± 10 CVs with $L_X(0.5\text{--}2.0\text{ keV}) \gtrsim 10^{30}\text{ erg s}^{-1}$ translates to a space density of $\sim 1.3 \times 10^{-6}\text{ pc}^{-3}$ considering the cluster mass ($\sim 3 \times 10^6\text{ M}_\odot$) and assuming $0.1\text{ M}_\odot/\text{pc}^{-3}$ in the solar neighborhood. This is a factor of three below the space density in the field, although it is within 2σ of the field value. However, the field estimate takes account of non-magnetic CVs only,¹² while there are hints that several of the CVs in ω Cen may be magnetic (see below), which would increase the apparent discrepancy. We conclude that ω Cen has fewer CVs per unit mass than the field.¹³ It seems unlikely that the central densities in ω Cen are sufficiently high to destroy CVs, or even (wider-orbit) CV progenitors;

for instance, Ivanova et al. (2006) find a similar or larger number of CVs per unit mass in their simulation of a cluster of similar density to ω Cen, compared to the field. The reduction in CVs per unit mass might be due to a lower initial binary fraction in ω Cen than the field, and/or to effects of lower metallicity and larger age. These issues will be studied in more detail in Heinke et al. 2018, in prep.

Additional insight into the CVs in ω Cen comes from spectral fits to the brightest sources in the cluster (see Table 2). Hydrogen columns significantly above the cluster value were required to obtain good fits for six of the nine CVs in this list. The n_H values implied for these sources range from $\sim 4 \times 10^{21}\text{ cm}^{-2}$ to $2 \times 10^{22}\text{ cm}^{-2}$. Comparably large n_H values were found by Heinke et al. (2005) for four CVs in 47 Tuc (see their Fig. 17), three of which are known to be eclipsing systems. Thus it is possible that at least some of the high- n_H CVs in ω Cen are also high-inclination systems. From a statistical point of view, however, it would be surprising if 2/3 of the brightest CVs in ω Cen were all edge-on. An alternative explanation could be that at least some are magnetic. Intermediate polars, also known as DQ Her systems, are often found to require internal absorption (Norton & Watson 1989; Patterson 1994; Mukai 2017). These moderately magnetic systems are also brighter on average than non-magnetic systems (Pretorius et al. 2013), which could help explain why so many of the bright CVs in ω Cen display this feature.

One of the sources associated with an RGB/SGB-a star also shows enhanced absorption over the cluster value (see Table 2). These are stars that, in colour-magnitude diagrams, lie along the metal-rich anomalous subgiant and giant branches in ω Cen (Cool et al. 2013), hence the designation. It is currently unknown, however, whether they have chemical compositions that actually make them part of this population. If instead their metallicities are characteristic of one of the more metal-poor populations in ω Cen, then they are sub-subgiants (Mathieu et al. 2003; Geller et al. 2017a,b; Leiner et al. 2017) or, in the case of brighter members of the group, red stragglers. In this context the enhanced emission associated with the possible sub-subgiant (SSG) 34b is interesting given that enhanced absorption has been found to be associated with a number of other such systems (Mathieu et al. 2003) and multiple mechanisms put forward to explain SSGs involve mass loss and/or mass transfer (Leiner et al. 2017). Spectroscopic follow-up on this and other members of this population in ω Cen is needed to distinguish between these possibilities.

A class of objects that appears conspicuously absent from ω Cen is millisecond pulsars (MSPs). In contrast to 47 Tuc, which hosts 25 known MSPs (Freire et al. 2017), none has yet been detected in ω Cen. This may not be surprising, considering the role that stellar interactions are likely to play in the formation of MSPs in globular clusters (Heinke 2010), and the fact that the rate of interactions in ω Cen is more than an order of magnitude below that of 47 Tuc (Bahramian et al. 2013). NGC 6397, with an interaction rate comparable to that of ω Cen, has just one known MSP. On the other hand, gamma-ray emission from the cluster centre detected with *Fermi*/LAT (Abdo et al. 2010) hints at the presence of a small population of MSPs, formally estimated at 19 ± 9 . Thus it is of interest to ask whether the present X-ray observations can tell us anything about the possibility that some MSPs could exist in ω Cen and have somehow eluded detection. The known MSPs in 47 Tuc occupy a relatively small region of the X-ray CMD (see Fig. 10 of

likely to be present in the field (Pretorius & Knigge 2012) and presumably also in ω Cen, but at present are not well constrained.

¹¹ These figures were determined based on turnoff stars in the ACS/WFC data described by Cool et al. (2013).

¹² Including magnetic CVs in this estimate increases the numbers by a factor of ~ 1.2 (Pretorius et al. 2013).

¹³ This conclusion applies to CVs with $L_X > 10^{30}\text{ erg s}^{-1}$. Fainter CVs are

Heinke et al. 2005); the large majority have $L_x = 10^{30} - 10^{31}$ erg s^{-1} and X-ray colours that place them between the 0.5 and 3.0 keV *vmekal* models.¹⁴ The equivalent region in ω Cen (see Fig. 7a), contains ~ 40 sources, all but 5 of which are unidentified. Thus the present observations leave open the possibility that some MSPs could exist in ω Cen. However, given that multiple source types including CVs and active binaries also occupy this region of the X-ray CMD, radio detections are required to determine whether any of these sources are in fact MSPs.

Finally, we identify the first candidate symbiotic star in a globular cluster with 94a, the second brightest X-ray source in ω Cen. In section 6 above, the nature (a carbon-rich red giant, or CH star) and membership in the cluster of the optical counterpart are secured. In section 7, the X-ray spectrum of 94a is reasonably fit with a plasma temperature of 5 keV and intrinsic absorption of 7×10^{21} cm $^{-2}$. Although the first well-studied symbiotic stars tended to show quite soft spectra (e.g. Muerstet et al. (1997) using *ROSAT* data), recent studies of symbiotic stars have revealed that many have hard X-ray spectra (temperatures 5-50 keV), with substantial ($\sim 10^{22} - 10^{23}$ cm $^{-2}$) absorption (e.g. Luna et al. 2013). Thus, 94a's X-ray spectrum is quite consistent with those of symbiotic stars. No high-temperature emission lines have yet been identified from this star. However, as laid out clearly by Mukai et al. (2016) and also Hynes et al. (2014), van den Berg et al. (2006), and Munari & Zwitter (2002), symbiotic stars will only show strong optical emission lines if a very large ($> 4 \times 10^{34}$ erg s^{-1}) ionizing source is present. Thus, most symbiotic stars, including many with substantial ($> 10^{32}$ erg s^{-1}) X-ray luminosity, will not show strong optical emission lines. So from the optical perspective as well, 94a's properties are in line with our current understanding of symbiotic stars. We note that the relative rarity of symbiotic stars in globular clusters, compared to closer binaries, is a natural consequence of the wider orbits of symbiotic stars. Such binaries would be disrupted in the dense cores of globular clusters, so symbiotic stars should be produced only from primordial binaries in the low-density haloes of (preferentially massive) globular clusters.

9 SUMMARY

Analysis of a deep *Chandra* exposure of the globular cluster Omega Centauri has revealed 233 X-ray sources in the ACIS-I field of view, of which 95 are newly reported here. An estimated 60 ± 20 of these sources are cluster members, the remaining being primarily AGN. Among 45 sources with firm or tentative optical identifications are 18 CVs and CV candidates. Extrapolating from these, we estimate that the cluster contains $\sim 30 - 40$ CVs with $L_x \gtrsim 10^{30}$ erg s^{-1} , a factor of about three fewer than would be expected if ω Cen produced CVs at the same rate as the field. In contrast to other GCs with significant populations of known CVs, the majority of CVs in ω Cen lie outside the cluster core. Given ω Cen's very long half-mass relaxation time, this strongly suggests that a majority of ω Cen's CVs have evolved from primordial binaries. The two brightest CVs lie close to the cluster centre, hinting that a dynamical formation channel may also be active. Spectral analysis shows that five of the nine brightest CVs have significant internal absorption indicative of a possible magnetic nature. An X-ray CMD contains numerous unidentified sources with colours and luminosities typical of MSPs.

¹⁴ These colour boundaries are chosen for convenience of comparing to X-ray sources in ω Cen, not because MSPs are well fit by *vmekal* models.

Radio identifications are needed to determine whether any of these objects are MSPs and could help explain the gamma-ray emission seen from the central regions of the cluster (Abdo et al. 2010). Finally, we identify the second-brightest X-ray source present as a symbiotic star, the first such binary system found in a globular cluster.

10 ACKNOWLEDGEMENTS

We thank B. Luo for sharing results of the 2 Msec *Chandra* Deep Field South study. Support for this work was provided by the National Aeronautics and Space Administration through *Chandra* Award Number GO0-1040A issued by the *Chandra* X-ray Observatory Center, which is operated by the Smithsonian Astrophysical Observatory for and on behalf of the National Aeronautics Space Administration under contract NAS8-03060. DH acknowledges support from a Natural Sciences and Engineering Research Council of Canada (NSERC) Discovery Grant and a Fonds de recherche du Québec - Nature et Technologies (FRQNT) Nouveaux Chercheurs Grant. CH is supported by an NSERC Discovery Grant and an Accelerator Supplement.

REFERENCES

- Abdo A. A., et al., 2010, *A&A*, **524**, A75
- Anderson J., 2002, in van Leeuwen F., Hughes J. D., Piotto G., eds, *Astronomical Society of the Pacific Conference Series Vol. 265, Omega Centauri, A Unique Window into Astrophysics*. p. 87
- Anderson J., van der Marel R. P., 2010, *ApJ*, **710**, 1032
- Bahramian A., Heinke C. O., Sivakoff G. R., Gladstone J. C., 2013, *ApJ*, **766**, 136
- Bahramian A., Heinke C. O., Degenaar N., Chomiuk L., Wijnands R., Strader J., Ho W. C. G., Pooley D., 2015, *MNRAS*, **452**, 3475
- Bassa C., et al., 2004, *ApJ*, **609**, 755
- Baumgardt H., 2017, *MNRAS*, **464**, 2174
- Bekki K., Freeman K. C., 2003, *MNRAS*, **346**, L11
- Bellini A., et al., 2009, *A&A*, **493**, 959
- Bellini A., Anderson J., van der Marel R. P., King I. R., Piotto G., Bedin L. R., 2017, *ApJ*, **842**, 7
- Belloni D., Giersz M., Askar A., Leigh N., Hypki A., 2016, *MNRAS*, **462**, 2950
- Bogdanov S., van den Berg M., Heinke C. O., Cohn H. N., Lugger P. M., Grindlay J. E., 2010, *ApJ*, **709**, 241
- Cardelli J. A., Clayton G. C., Mathis J. S., 1989, *ApJ*, **345**, 245
- Carson J. E., Cool A. M., Grindlay J. E., 2000, *ApJ*, **532**, 461
- Cash W., 1979, *ApJ*, **228**, 939
- Cohn H. N., et al., 2010, *ApJ*, **722**, 20
- Cool A. M., Haggard D., Carlin J. L., 2002, in van Leeuwen F., Hughes J. D., Piotto G., eds, *Astronomical Society of the Pacific Conference Series Vol. 265, Omega Centauri, A Unique Window into Astrophysics*. p. 277
- Cool A. M., Haggard D., Arias T., Brochmann M., Dorfman J., Gafford A., White V., Anderson J., 2013, *ApJ*, **763**, 126
- D'Souza R., Rix H. W., 2013, *MNRAS*, **429**, 1887
- Davies M. B., 1997, *MNRAS*, **288**, 117
- Davies M. B., Benz W., 1995, *MNRAS*, **276**, 876
- Dempsey R. C., Linsky J. L., Schmitt J. H. M. M., Fleming T. A., 1993, *ApJ*, **413**, 333
- Dempsey R. C., Linsky J. L., Fleming T. A., Schmitt J. H. M. M., 1997, *ApJ*, **478**, 358
- Deveny S., et al., 2016, in *American Astronomical Society Meeting Abstracts*.
- Di Stefano R., Rappaport S., 1994, *ApJ*, **423**, 274

- Ferraro F. R., Sollima A., Rood R. T., Origlia L., Pancino E., Bellazzini M., 2006, *ApJ*, **638**, 433
- Freeman K. C., Rodgers A. W., 1975, *ApJ*, **201**, L71
- Freire P. C. C., et al., 2017, *MNRAS*, **471**, 857
- Geller A. M., et al., 2017a, *ApJ*, **840**, 66
- Geller A. M., Leiner E. M., Chatterjee S., Leigh N. W. C., Mathieu R. D., Sills A., 2017b, *ApJ*, **842**, 1
- Gendre B., Barret D., Webb N. A., 2003, *A&A*, **400**, 521
- Giacconi R., et al., 2001, *ApJ*, **551**, 624
- Gratton R., Sneden C., Carretta E., 2004, *ARA&A*, **42**, 385
- Gregory P. C., Lored T. J., 1992, *ApJ*, **398**, 146
- Grindlay J. E., Heinke C. O., Edmonds P. D., Murray S. S., Cool A. M., 2001, *ApJ*, **563**, L53
- Haggard D., Cool A. M., Anderson J., Edmonds P. D., Callanan P. J., Heinke C. O., Grindlay J. E., Bailyn C. D., 2004, *ApJ*, **613**, 512
- Haggard D., Cool A. M., Davies M. B., 2009, *ApJ*, **697**, 224
- Haggard D., Cool A. M., Heinke C. O., van der Marel R., Cohn H. N., Lugger P. M., Anderson J., 2013, *ApJL*, **773**, L31
- Harding G. A., 1962, *The Observatory*, **82**, 205
- Harris W. E., 2010, preprint, ([arXiv:1012.3224](https://arxiv.org/abs/1012.3224))
- Hasinger G., et al., 2001, *A&A*, **365**, L45
- Heinke C. O., 2010, in Kalogera V., van der Sluys M., eds, *American Institute of Physics Conference Series Vol. 1314*, American Institute of Physics Conference Series. pp 135–142 ([arXiv:1101.5356](https://arxiv.org/abs/1101.5356)), doi:10.1063/1.3536355
- Heinke C. O., Grindlay J. E., Edmonds P. D., Cohn H. N., Lugger P. M., Camilo F., Bogdanov S., Freire P. C., 2005, *ApJ*, **625**, 796
- Heinke C. O., et al., 2014, *MNRAS*, **444**, 443
- Hertz P., Grindlay J. E., 1983, *ApJ*, **275**, 105
- Hong J., van den Berg M., Schlegel E. M., Grindlay J. E., Koenig X., Laycock S., Zhao P., 2005, *ApJ*, **635**, 907
- Hong J., Vesperini E., Belloni D., Giersz M., 2017, *MNRAS*, **464**, 2511
- Hynes R. I., et al., 2014, *ApJ*, **780**, 11
- Ivanova N., Heinke C. O., Rasio F. A., Taam R. E., Belczynski K., Fregeau J., 2006, *MNRAS*, **372**, 1043
- Johnston H. M., Verbunt F., Hasinger G., 1994, *A&A*, **289**, 763
- Kaluzny J., Kubiak M., Szymanski M., Udalski A., Krzeminski W., Mateo M., 1996, *A&AS*, **120**, 139
- Kaluzny J., Olech A., Thompson I. B., Pych W., Krzemiński W., Schwarzenberg-Czerny A., 2004, *A&A*, **424**, 1101
- Kenyon S. J., 1986, *The Symbiotic Stars*. Cambridge University Press
- Kim D.-W., et al., 2004, *ApJ*, **600**, 59
- Lebzelter T., Wood P. R., 2016, *A&A*, **585**, A111
- Lee Y.-W., Joo J.-M., Sohn Y.-J., Rey S.-C., Lee H.-C., Walker A. R., 1999, *Nature*, **402**, 55
- Leiner E., Mathieu R. D., Geller A. M., 2017, *ApJ*, **840**, 67
- Lub J., 2002, in van Leeuwen F., Hughes J. D., Piotto G., eds, *ASPC Vol. 265, Omega Centauri, A Unique Window into Astrophysics*. p. 95
- Lugger P. M., Cohn H. N., Cool A. M., Heinke C. O., Anderson J., 2017, *ApJ*, **841**, 53
- Luna G. J. M., Sokoloski J. L., Mukai K., Nelson T., 2013, *A&A*, **559**, A6
- Luo B., et al., 2008, *ApJS*, **179**, 19
- Mathieu R. D., van den Berg M., Torres G., Latham D., Verbunt F., Stassun K., 2003, *AJ*, **125**, 246
- Mayor M., et al., 1997, *AJ*, **114**, 1087
- McClure R. D., 1984, *ApJ*, **280**, L31
- McClure R. D., Woodworth A. W., 1990, *ApJ*, **352**, 709
- McDonald I., van Loon J. T., Decin L., Boyer M. L., Dupree A. K., Evans A., Gehrz R. D., Woodward C. E., 2009, *MNRAS*, **394**, 831
- Muerset U., Wolff B., Jordan S., 1997, *A&A*, **319**, 201
- Mukai K., 2017, *PASP*, **129**, 062001
- Mukai K., et al., 2016, *MNRAS*, **461**, L1
- Munari U., Zwitter T., 2002, *A&A*, **383**, 188
- Nebot Gómez-Morán A., et al., 2013, *A&A*, **553**, A12
- Norris J. E., Da Costa G. S., 1995, *ApJ*, **447**, 680
- Norris J. E., Freeman K. C., Mighell K. J., 1996, *ApJ*, **462**, 241
- Norton A. J., Watson M. G., 1989, *MNRAS*, **237**, 853
- Núñez N. E., Nelson T., Mukai K., Sokoloski J. L., Luna G. J. M., 2016, *ApJ*, **824**, 23
- Park T., Kashyap V. L., Siemiginowska A., van Dyk D. A., Zezas A., Heinke C., Wargelin B. J., 2006, *ApJ*, **652**, 610
- Patterson J., 1994, *PASP*, **106**, 209
- Piotto G., et al., 2015, *AJ*, **149**, 91
- Pooley D., et al., 2003, *ApJL*, **591**, L131
- Pretorius M. L., Knigge C., 2012, *MNRAS*, **419**, 1442
- Pretorius M. L., Knigge C., Schwöpe A. D., 2013, *MNRAS*, **432**, 570
- Pryor C., Meylan G., 1993, in Djorgovski S. G., Meylan G., eds, *Astronomical Society of the Pacific Conference Series Vol. 50, Structure and Dynamics of Globular Clusters*. p. 357
- Rivera-Sandoval L. E., et al., 2018, *MNRAS*, in press
- Rodriguez C. L., Morscher M., Wang L., Chatterjee S., Rasio F. A., Spurzem R., 2016, *MNRAS*, **463**, 2109
- Rutledge R. E., Bildsten L., Brown E. F., Pavlov G. G., Zavlin V. E., 2002, *ApJ*, **578**, 405
- Tozzi P., et al., 2001, *ApJ*, **562**, 42
- Trager S. C., King I. R., Djorgovski S., 1995, *AJ*, **109**, 218
- Verbunt F., Johnston H. M., 2000, *A&A*, **358**, 910
- Verbunt F., Meylan G., 1988, *A&A*, **203**, 297
- Wang L., et al., 2016, *MNRAS*, **458**, 1450
- Weldrake D. T. F., Sackett P. D., Bridges T. J., 2007, *AJ*, **133**, 1447
- Wilms J., Allen A., McCray R., 2000, *ApJ*, **542**, 914
- van Leeuwen F., Le Poole R. S., Reijns R. A., Freeman K. C., de Zeeuw P. T., 2000, *A&A*, **360**, 472
- van Loon J. T., van Leeuwen F., Smalley B., Smith A. W., Lyons N. A., McDonald I., Boyer M. L., 2007, *MNRAS*, **382**, 1353
- van den Berg M., et al., 2006, *ApJ*, **647**, L135

Table 3. Omega Cen X-ray Sources

Src ^a	Position ^b	Error ^c (arcsec)	Offset ^d (r_c)	Counts Detected/Corrected			$\log \left(\frac{X_{soft}}{X_{hard}} \right)$	f_x (10^{-16} erg cm $^{-2}$ s $^{-1}$)			f_x ratio ^e 2012/2000	Optical ID ^f
				X_{med}	X_{soft}	X_{hard}		0.5–4.5 keV	0.5–6.0 keV	0.5–2.0 keV		
				0.5–4.5 keV	0.5–1.5 keV	1.5–6.0 keV		0.5–4.5 keV	0.5–6.0 keV	0.5–2.0 keV		
11a	J132641.506–472832.70	0.49	0.39	11/10.0	6/5.1	6/5.7	−0.04	4.3	5.9	3.9	1.37	...
11b	J132641.021–472737.30	0.33	0.60	173/183.2	97/94.9	80/96.5	−0.01	79.6	104.3	51.4	1.47	NV371
11d	J132640.786–472832.80	0.46	0.43	14/13.6	12/11.1	2/1.4	0.90	6.0	7.5	4.7
11e	J132643.279–472816.18	0.43	0.32	15/14.6	9/8.3	8/8.3	0.00	6.3	9.1	3.6
11f	J132642.670–472723.56	0.49	0.61	12/11.7	7/6.7	5/4.5	0.17	5.0	6.3	4.1
12a	J132648.643–472744.46	0.36	0.41	35/36.8	23/22.6	12/13.3	0.23	16.0	20.1	10.4	0.07	CV
12b	J132652.514–472737.70	0.33	0.56	116/133.9	56/60.0	69/91.9	−0.19	56.4	79.0	32.7	0.48	...
12c	J132647.945–472810.74	0.41	0.23	16/15.5	10/9.4	6/5.6	0.22	6.6	8.6	4.0
13a	J132653.506–472900.17	0.29	0.42	1860/2140.1	589/622.3	1464/1955.6	−0.50	914.0	1311.3	429.7	1.17	CV
13b	J132650.563–472918.19	0.33	0.30	17/92.8	5/24.2	14/87.4	−0.56	34.2	48.4	16.8	1.43	...
13c	J132652.126–472935.45	0.29	0.45	2042/3004.5	782/1047.9	1470/2471.0	−0.37	1238.5	1774.5	638.1	1.68	CV
13d	J132649.574–472924.18	0.36	0.29	6/34.4	6/32.9	0/0.0	...	16.0	20.3	13.9	0.97	...
13e	J132646.246–472948.27	0.42	0.40	15/17.0	13/14.3	2/1.1	1.11	6.9	8.8	5.3	0.65	...
13f	J132645.984–472916.32	0.34	0.21	17/67.9	6/21.5	14/64.5	−0.48	38.7	58.8	21.3	3.08	CV?
13g	J132654.065–472859.06	0.41	0.45	16/16.9	9/9.4	7/7.2	0.12	7.4	9.1	4.8
14c	J132644.062–472856.47	0.36	0.22	44/45.9	41/39.9	4/3.7	1.03	19.7	26.0	16.0	0.58	...
14d	J132638.016–472910.48	0.39	0.62	16/45.2	3/7.4	17/55.9	−0.88	21.2	34.3	9.0	1.36	...
14e	J132641.858–472923.03	0.55	0.42	7/7.5	2/1.8	5/6.2	−0.54	3.3	4.1	0.7
14f	J132639.154–472842.79	0.43	0.53	22/22.0	5/4.4	18/20.6	−0.67	9.5	12.6	4.4
21a	J132631.183–472827.57	0.43	1.06	58/62.0	15/14.5	44/54.5	−0.57	26.9	35.6	13.7	1.02	...
21c	J132636.852–472745.84	0.56	0.78	12/11.6	5/4.6	9/9.3	−0.31	5.0	7.3	2.5	0.80	...
21d	J132638.258–472740.12	0.38	0.73	59/62.4	27/26.5	35/42.0	−0.20	27.1	36.4	16.0	1.03	...
21e	J132645.206–472652.25	0.39	0.75	38/42.3	31/32.3	7/7.6	0.63	17.7	22.6	13.9	0.96	...
21f	J132637.860–472715.51	0.48	0.85	20/20.6	16/15.7	4/3.6	0.64	8.9	11.3	6.9
21g	J132640.776–472700.84	0.58	0.80	10/9.4	2/1.5	10/10.9	−0.86	4.0	6.2	1.3
22a	J132648.259–472640.76	0.52	0.81	12/11.8	7/6.5	5/5.1	0.11	5.2	6.5	2.5	0.76	(FGND)
22c	J132652.682–472713.10	0.32	0.70	179/212.6	96/105.8	97/133.4	−0.10	88.5	123.1	55.3	1.23	fbCV?
22d	J132658.723–472728.73	0.44	0.90	20/21.9	14/14.6	6/6.7	0.34	9.5	12.2	7.3	0.47	...
22e	J132659.930–472809.50	0.39	0.86	27/39.3	10/13.6	19/31.7	−0.37	17.8	24.4	12.5	0.45	RGB/SGB-a
22f	J132658.802–472820.90	0.36	0.77	51/68.3	23/28.7	29/44.3	−0.19	28.2	37.2	15.2	1.18	(AGN)
22g	J132646.181–472640.95	0.72	0.81	6/5.2	0/0.0	9/9.7	...	2.2	4.4	0.0
22h	J132657.638–472712.29	0.49	0.91	14/14.4	6/5.7	10/11.8	−0.31	6.1	9.1	3.4
22i	J132656.290–472806.82	0.53	0.65	6/7.2	5/6.2	1/0.1	1.96	3.5	4.3	2.6
22j	J132656.460–472815.67	0.46	0.64	10/11.3	8/8.9	2/1.6	0.76	5.0	6.1	3.8
22k	J132659.328–472829.08	0.65	0.80	6/5.3	1/0.6	8/8.9	−1.16	2.2	4.5	0.3
22l	J132654.828–472832.66	0.40	0.51	20/19.6	13/12.3	9/8.9	0.14	8.4	11.6	6.2
23a	J132651.050–473009.98	0.36	0.59	48/58.6	21/23.6	31/42.2	−0.25	24.3	33.6	15.3	0.54	...
23b	J132651.672–473047.21	0.47	0.83	19/18.5	5/4.4	14/15.2	−0.54	7.9	10.0	5.2	0.57	CV?
23d	J132658.476–472847.45	0.47	0.74	13/12.3	6/5.3	10/11.0	−0.32	5.2	8.4	3.1
23e	J132658.174–472957.10	0.55	0.85	9/9.8	7/7.6	4/3.9	0.29	4.2	6.5	3.3
23f	J132657.247–473012.74	0.55	0.86	9/10.3	6/6.5	3/3.1	0.33	4.6	5.7	3.0
23g	J132655.231–473011.63	0.46	0.76	14/15.8	12/13.2	3/2.8	0.68	6.7	9.2	5.5
23h	J132653.945–473036.11	0.55	0.83	11/10.5	9/8.5	2/0.9	0.97	4.4	5.5	3.6
24b	J132639.312–473037.06	0.50	0.88	20/20.0	14/13.4	6/5.6	0.38	8.6	10.9	6.0	1.02	...
24c	J132638.422–473036.53	0.40	0.92	71/76.1	34/33.8	41/49.7	−0.17	32.3	44.1	19.8	1.23	CV
24d	J132637.399–473006.97	0.49	0.83	20/21.2	14/14.3	6/6.1	0.37	9.2	11.9	6.4	0.98	...
24f	J132637.248–472942.37	0.45	0.75	20/26.0	17/21.2	8/10.8	0.29	11.1	17.8	8.6	1.72	RGB/SGB-a
24g	J132634.394–472955.46	0.39	0.95	82/93.7	41/43.2	50/65.2	−0.18	40.9	59.1	21.4	0.78	(AGN?)
24i	J132642.564–473022.49	0.49	0.69	16/15.8	1/0.4	20/23.1	−1.71	6.7	11.3	1.3
24j	J132642.326–473019.33	0.45	0.68	21/20.9	16/15.0	5/4.7	0.50	8.9	11.3	7.4
24k	J132635.422–472838.24	0.81	0.77	6/5.1	2/1.4	8/8.6	−0.78	2.4	5.3	1.0

Table 3 (cont'd)

Src ^a	Position ^b	Error ^c (arcsec)	Offset ^d (r_c)	Counts Detected/Corrected			$\log \left(\frac{X_{soft}}{X_{hard}} \right)$	f_x (10^{-16} erg cm ⁻² s ⁻¹)			f_x ratio ^e 2012/2000	Optical ID ^f
				X_{med}	X_{soft}	X_{hard}		0.5–4.5 keV	0.5–6.0 keV	0.5–2.0 keV		
				0.5–4.5 keV	0.5–1.5 keV	1.5–6.0 keV		0.5–4.5 keV	0.5–6.0 keV	0.5–2.0 keV		
31a	J132629.359–472813.08	0.40	1.19	119/136.9	51/54.1	79/105.7	−0.29	58.8	84.0	33.5	1.58	fbCV?
31b	J132631.414–472801.23	0.56	1.08	20/20.2	8/7.4	12/13.7	−0.27	8.9	11.3	5.7	1.01	(AGN)
31c	J132632.323–472707.93	0.60	1.16	17/18.3	12/12.4	5/4.9	0.40	7.9	9.8	6.9	0.45	...
31d	J132636.230–472621.77	0.42	1.18	74/83.6	32/33.6	46/59.9	−0.25	36.2	49.1	19.8	0.75	...
31e	J132630.415–472711.19	0.72	1.26	12/13.3	7/7.5	5/5.3	0.15	5.7	7.1	3.3
31f	J132630.470–472618.39	0.62	1.45	21/26.6	3/3.3	20/29.8	−0.95	11.3	16.2	1.8
31g	J132634.171–472641.86	0.63	1.17	14/15.4	9/9.6	6/6.8	0.15	6.5	8.9	5.0
32a	J132646.356–472518.21	0.55	1.35	22/25.6	6/6.2	17/23.1	−0.57	10.9	14.8	5.9	0.75	fbCV?
32b	J132652.162–472532.32	0.55	1.29	8/21.2	3/7.2	5/15.0	−0.32	8.8	11.3	4.7	1.03	...
32c	J132655.894–472602.06	0.44	1.20	38/40.9	10/9.8	34/42.8	−0.64	17.4	26.3	9.0	1.68	...
32d	J132702.422–472647.03	0.55	1.26	17/17.6	13/13.1	5/4.8	0.44	7.5	10.1	5.4	0.61	...
32f	J132705.328–472808.56	0.39	1.21	73/84.8	41/44.5	35/46.6	−0.02	36.0	48.7	25.1	1.55	RGB/SGB-a
32g	J132647.410–472549.21	0.71	1.14	9/8.8	5/4.7	4/4.0	0.08	3.7	4.8	3.0
32h	J132650.686–472512.94	0.48	1.40	36/47.0	20/24.1	17/25.1	−0.02	20.0	26.6	13.3
32i	J132658.752–472713.88	0.83	0.96	5/4.1	3/2.6	3/2.5	0.01	1.7	2.8	1.3
33b	J132706.478–472852.93	0.45	1.26	39/41.2	7/6.6	37/45.7	−0.84	17.4	25.6	7.5	1.08	...
33c	J132703.564–472857.59	0.65	1.07	9/8.0	4/3.3	6/6.0	−0.25	3.3	4.8	1.9	0.49	...
33d	J132701.500–472924.60	0.39	0.97	24/56.5	6/12.7	21/57.6	−0.66	22.9	33.3	13.7	0.96	...
33e	J132700.970–473004.42	0.43	1.03	28/32.8	14/15.4	16/20.7	−0.13	13.8	18.9	10.2	0.94	CV?
33f	J132659.280–473037.45	0.51	1.07	19/19.4	7/6.4	13/15.0	−0.37	8.1	10.9	4.4	0.65	...
33g	J132655.997–473045.87	0.59	0.96	11/10.3	10/9.5	1/0.0	...	4.4	5.5	3.7	0.60	...
33h	J132655.058–473113.25	0.35	1.08	247/271.2	93/93.6	174/218.5	−0.37	114.9	160.6	62.3	1.53	...
33i	J132651.070–473144.34	0.40	1.18	96/106.3	36/36.5	70/88.8	−0.39	45.2	64.7	25.1	0.49	...
33k	J132649.788–473147.66	0.41	1.18	65/87.7	30/37.2	40/61.4	−0.22	37.0	51.9	22.3	1.24	...
33l	J132648.725–473124.90	0.32	1.03	307/897.5	154/411.1	172/577.5	−0.15	366.5	505.1	221.2	2.74	(AGN?)
33m	J132646.500–473140.77	0.49	1.13	28/32.2	8/8.3	23/30.5	−0.56	13.5	19.4	6.2	1.17	CV?
33n	J132703.175–472901.10	0.90	1.05	5/4.0	2/1.5	4/3.8	−0.40	1.7	2.7	0.9
33o	J132700.106–473036.29	0.55	1.10	15/15.1	4/3.6	13/15.0	−0.62	6.4	9.3	2.1
33p	J132657.691–473021.51	0.68	0.92	6/6.5	2/1.8	4/4.5	−0.40	2.8	3.4	1.6
33q	J132652.366–473153.45	0.76	1.25	10/9.9	4/3.6	6/6.5	−0.25	4.4	5.5	3.0
34b	J132637.421–473052.75	0.39	1.04	87/103.5	30/32.6	63/86.4	−0.42	46.2	63.8	25.6	0.32	RGB/SGB-a
34d	J132634.330–473032.98	0.43	1.09	56/64.1	16/16.8	47/62.2	−0.57	26.6	39.2	13.0	0.35	...
34e	J132643.202–473110.62	0.51	0.97	21/21.0	12/11.3	9/9.3	0.09	8.9	11.3	6.0
34f	J132631.711–473105.93	0.85	1.36	10/11.5	5/5.5	5/5.9	−0.03	4.9	6.1	2.6
34g	J132631.877–473101.63	0.78	1.33	12/13.4	2/1.8	12/15.9	−0.95	5.6	8.6	1.5
34h	J132631.344–472932.22	0.61	1.08	15/16.8	9/9.6	7/8.3	0.06	7.0	9.6	4.5
41a	J132624.398–472657.40	0.56	1.65	50/56.8	25/26.9	28/36.1	−0.13	24.7	34.2	13.6	1.27	...
41c	J132624.535–472610.61	0.62	1.79	44/52.6	15/16.5	30/41.4	−0.40	22.8	30.2	10.2	1.09	...
41d	J132628.644–472627.04	0.38	1.51	360/407.5	73/76.5	334/438.9	−0.76	177.7	262.5	65.7	1.17	CV
41e	J132630.547–472600.81	0.60	1.53	34/34.7	28/28.3	7/5.4	0.72	15.1	19.9	12.3	1.06	...
41f	J132632.016–472451.22	0.48	1.82	102/140.2	52/67.5	56/88.3	−0.12	59.0	82.8	36.7	1.44	...
41g	J132637.339–472430.15	0.57	1.78	41/58.4	22/29.9	23/36.8	−0.09	25.5	36.9	17.6	0.73	(AGN)
41i	J132623.921–472731.35	0.91	1.60	15/14.4	4/3.4	11/11.6	−0.53	6.1	7.8	3.3
41j	J132624.307–472646.93	0.84	1.69	18/19.4	6/6.3	13/15.0	−0.38	8.6	11.4	5.1
41k	J132630.958–472521.71	0.66	1.70	30/32.7	19/20.7	13/14.5	0.15	14.3	19.7	9.8
41l	J132636.413–472528.70	0.76	1.46	12/14.7	7/8.2	7/9.7	−0.07	6.1	9.6	4.2
42a	J132701.651–472543.35	0.72	1.51	11/13.9	5/5.9	7/9.9	−0.23	5.7	8.1	4.7	0.34	...
42d	J132649.128–472450.90	0.61	1.53	17/25.1	14/19.6	3/4.0	0.69	10.4	14.0	9.0
43a	J132707.956–472944.51	0.46	1.41	17/50.2	9/24.7	8/26.2	−0.03	21.2	26.8	13.6	0.84	...
43c	J132706.890–473008.85	0.53	1.39	22/27.0	10/11.4	12/16.3	−0.16	11.2	14.4	7.0	1.00	RGB/SGB-a
43d	J132704.495–473037.64	0.42	1.34	72/80.7	27/28.0	50/63.9	−0.36	33.7	47.1	17.6	1.16	...

Table 3 (cont'd)

Src ^a	Position ^b	Error ^c (arcsec)	Offset ^d (r _c)	Counts Detected/Corrected			$\log\left(\frac{X_{soft}}{X_{hard}}\right)$	f_x (10 ⁻¹⁶ erg cm ⁻² s ⁻¹)			f_x ratio ^e 2012/2000	Optical ID ^f
				X_{med}	X_{soft}	X_{hard}		0.5–4.5 keV	0.5–6.0 keV	0.5–2.0 keV		
				0.5–4.5 keV	0.5–1.5 keV	1.5–6.0 keV		0.5–4.5 keV	0.5–6.0 keV	0.5–2.0 keV		
43f	J132656.014–473202.05	0.61	1.39	19/21.3	14/14.9	5/5.2	0.45	8.7	11.4	7.0	0.39	(FGND)
43h	J132649.582–473212.70	0.37	1.34	208/290.8	96/122.7	128/207.2	−0.23	121.4	171.7	68.7	1.75	CV?
43i	J132704.666–473008.55	0.69	1.26	9/10.0	0/0.0	12/15.6	...	4.2	7.2	0.0
43j	J132705.256–473015.81	0.57	1.31	13/18.9	8/11.2	6/9.0	0.09	7.8	10.8	5.8
43k	J132701.380–473059.64	0.61	1.26	15/15.1	4/3.5	17/20.3	−0.76	6.3	11.8	2.9
43l	J132657.187–473134.17	0.66	1.26	13/13.5	2/1.7	12/14.3	−0.92	5.6	7.9	1.5
43m	J132652.704–473210.42	0.91	1.36	8/8.4	3/2.8	6/7.1	−0.40	3.3	5.1	1.5
44a	J132644.110–473230.86	0.39	1.46	176/271.0	105/148.4	79/142.4	0.02	112.0	156.2	76.9	0.51	...
44b	J132633.468–473153.25	0.64	1.50	26/29.1	4/3.4	27/35.1	−1.01	12.6	19.2	3.9	0.75	...
44c	J132623.674–473044.56	0.94	1.72	16/16.9	2/1.7	15/18.2	−1.03	7.4	9.9	3.2	0.41	fbCV?
44d	J132622.886–473008.58	0.65	1.68	36/39.2	16/16.4	26/32.1	−0.29	16.5	25.8	10.4	0.56	CV?
44e	J132619.793–472910.32	0.38	1.80	882/1066.4	754/859.2	129/174.8	0.69	463.3	600.0	385.9	0.71 ^g	qLMXB
44f	J132626.616–473025.17	1.01	1.49	12/10.5	2/1.2	12/12.7	−1.02	4.3	6.7	1.0
51a	J132631.286–472439.00	0.56	1.91	65/82.0	26/31.5	46/64.6	−0.31	36.6	51.8	17.9	0.69	...
51b	J132630.614–472346.31	1.21	2.22	18/18.2	5/5.0	15/15.7	−0.50	7.7	10.5	4.5	0.59	...
51d	J132640.980–472401.75	0.47	1.88	130/164.4	52/62.3	81/118.4	−0.28	70.7	95.3	45.9	1.90	...
51e	J132644.724–472333.32	0.94	2.03	22/20.4	14/14.4	8/4.6	0.50	8.8	10.7	7.2	0.62	(FGND)
51f	J132629.460–472403.01	1.18	2.17	19/18.0	3/2.1	24/28.9	−1.14	7.6	15.2	2.4
52c	J132706.394–472537.90	0.46	1.75	93/105.0	42/44.2	63/83.0	−0.27	45.0	66.0	22.5	0.79	(AGN?)
52d	J132714.993–472743.49	0.68	1.86	24/27.4	10/10.9	18/23.6	−0.33	12.0	18.1	7.0	0.84	fbCV?
52e	J132717.066–472819.07	0.47	1.96	114/143.5	45/53.0	81/120.1	−0.36	60.3	88.0	32.6	4.51	...
52f	J132714.395–472830.55	0.57	1.78	34/43.3	22/26.9	12/16.7	0.21	18.2	23.8	12.1	0.80	...
52g	J132717.698–472748.52	0.74	2.03	24/29.2	15/18.1	9/10.6	0.23	12.5	15.5	9.5
53a	J132659.767–473237.12	0.74	1.70	19/21.2	14/15.7	7/6.7	0.37	9.0	12.7	6.4	0.45	...
53c	J132701.651–473259.99	1.04	1.89	13/13.6	6/6.4	7/6.4	0.00	5.7	6.9	2.7
53d	J132700.163–473303.61	0.91	1.86	15/17.3	9/10.6	6/5.3	0.31	7.0	8.6	5.2
54b	J132642.461–473308.93	0.48	1.72	103/121.5	13/13.7	112/153.6	−1.05	52.5	83.0	18.0	1.60	fbCV?
54c	J132627.050–473215.02	0.48	1.89	153/195.2	31/36.7	137/202.2	−0.74	88.1	124.9	37.5	2.89	...
54d	J132625.128–473227.15	0.46	2.03	224/346.1	107/155.2	137/245.9	−0.20	156.1	221.5	99.2	0.71	(AGN)
54f	J132621.898–473049.42	0.86	1.84	26/24.7	18/17.9	11/7.8	0.36	10.7	14.7	7.3	0.98	...
54g	J132620.138–473015.69	0.87	1.86	29/25.0	12/10.0	18/16.2	−0.21	10.8	14.0	6.7	2.14	(AGN)
54h	J132620.362–473002.68	0.42	1.83	394/434.3	139/142.7	301/384.2	−0.43	191.1	276.5	97.3	0.54	CV
54i	J132623.978–473159.12	1.48	1.96	15/10.7	4/1.8	15/13.9	−0.89	4.5	7.8	1.3
54j	J132622.716–473212.60	1.15	2.08	19/19.3	5/3.5	16/20.7	−0.77	8.2	12.0	2.1
54k	J132617.566–473052.63	1.11	2.10	22/21.4	8/7.3	14/13.3	−0.26	8.9	10.8	5.0
54l	J132616.634–473053.66	0.62	2.16	66/113.6	24/39.2	51/103.6	−0.42	48.5	74.9	24.6
54m	J132615.161–473021.83	1.19	2.19	27/21.0	16/14.0	15/10.7	0.12	9.4	13.8	6.1
54n	J132617.266–472951.50	1.26	2.01	19/15.0	15/14.3	5/0.0	...	6.6	8.5	5.2
61a	J132620.930–472448.22	0.97	2.31	33/34.2	8/7.2	34/42.4	−0.77	14.9	25.2	4.2	3.32	...
61b	J132641.510–472216.08	0.52	2.55	274/388.7	74/107.1	234/383.4	−0.55	173.7	260.5	82.0	1.03	...
61c	J132612.600–472831.80	1.08	2.27	20/28.3	6/2.4	17/35.4	−1.16	11.4	18.5	3.2
61d	J132610.219–472657.68	1.27	2.52	30/28.1	9/7.2	26/28.9	−0.60	12.4	18.9	5.8
62a	J132648.437–472216.95	0.70	2.52	69/92.1	27/38.3	51/74.4	−0.29	41.3	59.1	20.6	2.92	...
62b	J132707.990–472333.64	0.51	2.43	195/270.7	64/87.4	141/229.4	−0.42	112.6	159.4	58.7	1.45	(AGN)
62c	J132712.415–472423.95	0.68	2.36	52/66.8	22/28.0	36/53.0	−0.28	28.6	40.9	14.9	1.03	...
62d	J132716.253–472457.73	0.80	2.41	24/45.5	20/39.6	4/0.6	1.83	18.1	22.7	14.4	0.93	...
62e	J132723.978–472819.07	0.96	2.41	24/28.9	7/8.1	21/29.2	−0.56	11.9	18.4	7.1	0.68	...
62f	J132706.386–472315.61	1.06	2.48	28/26.9	4/2.5	28/32.6	−1.12	11.4	17.3	5.4
62g	J132707.488–472345.08	1.01	2.35	23/24.9	12/13.8	12/12.1	0.06	10.6	13.6	7.6
62h	J132719.939–472550.10	1.12	2.42	20/21.3	6/5.5	16/20.1	−0.56	8.7	12.5	4.7
63a	J132722.918–472907.38	1.06	2.34	22/21.4	5/4.4	23/26.7	−0.78	9.0	15.0	3.7	0.33	...

Table 3 (cont'd)

Src ^a	Position ^b	Error ^c (arcsec)	Offset ^d (r _c)	Counts Detected/Corrected			$\log\left(\frac{X_{soft}}{X_{hard}}\right)$	f_x (10 ⁻¹⁶ erg cm ⁻² s ⁻¹)			f_x ratio ^e 2012/2000	Optical ID ^f
				X_{med}	X_{soft}	X_{hard}		0.5–4.5 keV	0.5–6.0 keV	0.5–2.0 keV		
				0.5–4.5 keV	0.5–1.5 keV	1.5–6.0 keV		0.5–4.5 keV	0.5–6.0 keV	0.5–2.0 keV		
63b	J132714.623–473150.71	0.55	2.15	99/115.8	16/17.0	97/130.7	–0.89	48.8	71.5	18.0	1.51	...
63c	J132711.750–473240.79	0.51	2.20	153/178.4	61/67.0	106/141.0	–0.32	74.2	105.4	41.4	0.22	...
63d	J132710.030–473320.24	0.54	2.31	126/177.0	28/36.1	123/202.8	–0.75	73.1	115.7	27.4	0.70	...
63e	J132701.932–473355.31	1.07	2.21	18/21.3	3/2.5	19/26.9	–1.03	9.3	14.4	0.8	0.55	...
63f	J132657.175–473351.85	0.99	2.08	20/21.0	18/21.5	4/0.0	...	8.9	12.3	8.1	0.64	...
63g	J132656.683–473427.68	0.76	2.29	47/56.1	4/3.1	49/68.8	–1.34	23.6	34.4	11.6	1.26	...
63h	J132721.562–472920.91	1.04	2.26	21/19.6	18/19.3	3/0.0	...	8.3	9.5	7.2	...	(NV410)
63i	J132712.418–473251.55	1.03	2.28	22/23.5	1/0.0	24/31.4	...	9.7	13.9	0.1
64a	J132627.012–473407.75	0.69	2.46	100/119.8	25/28.1	86/119.4	–0.63	51.6	75.4	23.6	0.56	...
64b	J132624.437–473302.58	0.90	2.23	39/39.1	2/0.0	51/64.6	...	17.3	31.3	2.2	0.68	...
64c	J132616.279–473058.39	0.64	2.20	59/105.1	30/51.6	33/67.5	–0.12	42.0	65.0	31.4	1.17	...
64d	J132614.038–473019.97	0.68	2.25	84/95.4	27/29.1	61/77.9	–0.43	42.3	56.3	19.2	2.80	...
64e	J132640.754–473450.95	1.16	2.39	25/26.1	2/0.0	28/35.8	...	10.7	16.8	2.7
64f	J132622.346–473319.09	1.41	2.40	21/20.1	16/18.1	7/1.8	1.01	8.4	11.5	7.6
71a	J132604.190–472805.61	1.63	2.83	37/26.9	16/14.8	23/13.5	0.04	12.6	15.2	7.7	0.94	...
71b	J132604.553–472741.47	0.78	2.82	118/150.7	56/81.6	73/102.5	–0.10	68.5	100.2	42.5	1.29	...
71c	J132612.758–472411.42	0.73	2.87	119/183.1	49/75.4	81/142.0	–0.27	79.3	114.8	47.4	0.96	...
71d	J132617.590–472337.26	0.99	2.78	57/64.4	18/18.9	51/67.2	–0.55	28.1	45.0	13.4	1.84	...
71e	J132623.124–472250.71	0.71	2.79	128/162.1	57/72.1	80/112.4	–0.19	71.7	99.5	43.8	1.38	...
71f	J132610.478–472558.74	1.53	2.64	30/23.2	14/13.6	27/22.3	–0.21	10.6	19.3	6.7
71g	J132633.403–472159.40	1.16	2.78	37/40.0	14/18.1	24/23.9	–0.12	18.3	22.5	11.5
71h	J132642.667–472125.76	1.63	2.86	30/22.9	9/7.7	25/18.3	–0.37	10.6	13.9	2.9
72a	J132648.007–472150.68	0.86	2.68	53/67.1	24/35.1	33/41.9	–0.08	29.8	40.9	19.2	1.66	...
72b	J132654.521–472204.63	0.48	2.64	214/693.1	91/320.7	139/513.6	–0.20	325.3	448.1	199.5	0.45	...
72d	J132723.304–472447.17	0.77	2.82	73/96.1	18/22.2	65/100.6	–0.66	39.0	60.0	17.3	0.97	...
73a	J132721.706–473206.73	0.74	2.60	69/81.7	47/57.2	24/25.6	0.35	34.4	45.7	26.4	0.69	NV369
73b	J132720.923–473233.65	1.19	2.65	31/28.0	16/16.8	17/12.0	0.14	11.5	15.4	7.1	0.42	...
73c	J132659.256–473457.75	0.54	2.52	249/312.5	94/113.0	170/245.3	–0.34	132.3	184.9	73.1	1.68	...
73d	J132647.316–473559.18	0.97	2.79	49/66.6	28/44.3	23/25.9	0.23	29.0	36.6	21.8	0.64	(V210)
73e	J132721.458–473221.21	1.30	2.63	27/23.3	3/0.0	31/34.5	...	10.0	16.2	1.2
74a	J132629.038–473436.90	1.00	2.56	39/47.6	25/32.2	15/14.0	0.36	19.9	26.0	13.1	0.98	...
74b	J132627.499–473455.37	0.58	2.71	263/374.1	114/160.1	169/273.8	–0.23	167.5	235.0	93.7	1.02	...
74c	J132617.285–473408.12	1.42	2.85	37/35.5	8/5.5	41/51.2	–0.97	15.6	28.6	2.4	0.97	...
74d	J132608.314–473032.85	1.04	2.64	56/52.2	25/24.3	33/32.5	–0.13	23.0	30.9	14.9	0.53	V216
74g	J132633.031–473449.33	1.48	2.52	20/20.8	2/0.0	22/28.1	...	9.1	12.9	1.5
81a	J132634.793–472055.39	1.70	3.15	31/30.6	16/24.3	20/15.7	0.19	14.0	21.0	11.3	0.81	...
81b	J132614.350–472241.71	1.59	3.19	33/39.6	9/10.5	33/46.7	–0.65	16.9	30.1	8.1
82b	J132710.181–472127.94	0.77	3.20	112/186.5	90/203.5	23/28.2	0.86	82.4	111.8	79.2	0.98	(NV377)
82c	J132718.026–472256.15	1.20	3.03	39/43.3	7/6.0	37/46.2	–0.89	18.8	26.0	5.8	0.80	...
82d	J132721.151–472323.35	0.64	3.05	199/277.3	92/132.9	120/188.4	–0.15	118.3	167.3	72.7	0.99	...
82e	J132728.366–472421.82	0.80	3.19	103/151.4	37/56.0	75/127.1	–0.36	63.8	92.6	34.6	0.61	...
82f	J132729.292–472553.77	0.69	2.97	140/178.8	53/68.3	95/138.5	–0.31	75.7	104.7	35.9	0.13	...
82g	J132730.629–472654.11	1.00	2.93	54/55.7	13/10.1	44/54.3	–0.73	23.4	32.0	7.2	0.70	...
82h	J132719.838–472250.40	1.10	3.14	50/61.0	5/4.4	57/84.1	–1.28	26.3	43.6	6.3
83a	J132727.410–473132.16	0.60	2.84	214/262.2	106/129.4	128/175.7	–0.13	112.3	159.5	73.0	0.49	...
83b	J132720.126–473336.01	1.18	2.85	38/38.3	12/11.5	31/35.7	–0.49	16.0	23.7	9.3	0.82	...
83c	J132722.834–473356.36	1.03	3.07	55/69.5	21/25.3	41/57.8	–0.36	28.8	41.7	18.0	0.57	...
83d	J132718.624–473403.83	0.98	2.90	52/63.8	10/10.0	54/77.7	–0.89	27.0	43.1	10.4	0.97	...
83e	J132712.857–473456.86	0.53	2.92	534/691.4	230/286.9	340/509.1	–0.25	293.0	415.3	175.3	0.60	...
83f	J132714.906–473531.05	0.95	3.18	80/106.7	13/14.6	99/163.2	–1.05	43.4	86.9	7.0
84a	J132639.202–473631.34	0.77	3.05	135/196.4	51/86.0	97/153.9	–0.25	88.6	128.6	54.6	0.72	...

Table 3 (cont'd)

Src ^a	Position ^b	Error ^c (arcsec)	Offset ^d (r_c)	Counts Detected/Corrected			$\log \left(\frac{X_{soft}}{X_{hard}} \right)$	f_x (10^{-16} erg cm ⁻² s ⁻¹)			f_x ratio ^e 2012/2000	Optical ID ^f
				X_{med}	X_{soft}	X_{hard}		0.5–4.5 keV	0.5–6.0 keV	0.5–2.0 keV		
				0.5–4.5 keV	0.5–1.5 keV	1.5–6.0 keV		0.5–4.5 keV	0.5–6.0 keV	0.5–2.0 keV		
84b	J132638.191–473636.39	0.96	3.09	78/107.0	29/48.5	54/76.5	−0.20	50.1	67.1	27.9	1.34	...
84c	J132613.620–473441.39	0.67	3.17	253/483.4	107/203.9	162/361.6	−0.25	212.8	309.4	128.8	1.06	...
84d	J132611.527–473402.82	0.69	3.10	240/375.9	169/269.1	78/132.0	0.31	164.2	227.2	129.5	0.51	(V167)
84f	J132600.881–472910.33	1.36	3.04	44/48.9	20/24.8	28/35.8	−0.16	21.9	31.3	14.4	0.73	...
84g	J132623.947–473611.72	0.74	3.25	198/345.9	67/127.5	155/307.8	−0.38	153.1	233.6	89.7
91a	J132618.708–472109.75	1.15	3.49	60/109.5	32/71.5	28/47.5	0.18	48.6	64.8	41.2	1.46	NV379
91c	J132606.754–472238.04	1.74	3.56	33/52.1	13/26.8	21/29.5	−0.04	23.6	30.6	19.7
92d	J132732.306–472510.43	1.29	3.26	29/49.0	7/9.7	25/46.0	−0.68	20.2	27.2	6.7
92e	J132737.622–472633.12	1.08	3.41	60/88.0	22/36.3	47/76.9	−0.33	37.4	58.2	22.1
93b	J132734.596–473237.58	0.75	3.44	177/306.3	68/133.7	124/240.5	−0.25	131.0	194.8	79.1	1.66	...
93c	J132700.310–473714.88	0.97	3.39	59/144.4	18/51.3	44/117.2	−0.36	65.6	89.3	43.2	0.90	...
93d	J132734.006–473147.43	1.07	3.27	59/79.7	24/36.7	39/53.9	−0.17	34.1	47.1	23.2
93e	J132725.042–473501.23	1.47	3.46	39/53.6	14/19.3	27/37.7	−0.29	20.7	29.4	12.3
93f	J132714.426–473559.83	1.27	3.31	47/62.7	13/16.5	43/67.7	−0.61	25.1	42.9	18.6
93g	J132709.665–473646.21	1.86	3.43	31/35.6	9/9.7	30/42.8	−0.65	16.0	27.1	9.9
93h	J132657.610–473703.11	1.46	3.28	35/48.5	15/27.6	27/36.0	−0.12	20.1	33.6	11.7
94a	J132601.579–473305.69	0.55	3.42	1018/2329.2	272/688.8	820/2167.1	−0.50	1006.0	1542.4	532.7	0.68	CH star
94b	J132557.374–473248.30	0.97	3.62	49/246.5	20/131.9	34/182.2	−0.14	107.6	155.9	58.0	0.41	...
94c	J132636.670–473729.45	1.01	3.45	47/155.9	5/16.8	50/182.6	−1.04	66.5	105.0	17.5
94d	J132613.992–473541.50	1.54	3.45	40/61.1	6/7.6	48/89.2	−1.07	26.8	50.7	10.5
94e	J132611.326–473559.04	1.15	3.65	90/153.6	32/62.5	67/121.4	−0.29	66.8	99.0	43.8
94f	J132610.774–473505.38	0.90	3.42	118/229.5	14/22.3	126/293.3	−1.12	93.7	163.6	21.6
94g	J132559.299–473349.48	1.64	3.69	47/72.9	14/25.9	41/71.8	−0.44	31.6	53.1	19.2
103a	J132733.187–473432.51	1.12	3.74	66/137.2	28/68.0	42/88.9	−0.12	55.4	82.4	39.5
103b	J132730.869–473429.09	1.64	3.61	35/50.5	11/17.4	26/35.3	−0.31	19.3	26.8	10.4
104b	J132611.489–473708.07	0.79	3.99	148/854.1	59/491.0	100/609.2	−0.09	401.2	582.4	259.2
104c	J132604.152–473513.36	1.87	3.76	43/60.5	17/31.1	35/51.6	−0.22	25.4	44.6	20.5
113a	J132729.333–473634.52	1.31	4.09	74/147.8	15/29.7	67/151.7	−0.71	60.0	93.9	26.8
113b	J132725.066–473655.24	2.46	4.01	30/40.0	10/15.7	23/26.3	−0.22	15.5	21.7	14.1

Note. — ^a Source IDs as assigned in this work (bold face) and in [Haggard et al. \(2009\)](#); ^b Source positions in the format JHHMMSS.ss–DDMMSS.ss; ^c 95% confidence error circle radius calculated using Eq.(5) of [Hong et al. \(2005\)](#); ^d Offset from [Anderson & van der Marel \(2010\)](#) cluster center (R.A. = 13:26:47.24, Dec. = −47:28:46.45) in units of the core radius (r_c = 155 arcsec); ^e Unabsorbed fluxes determined assuming a power-law spectrum with photon index Γ = 1.4; ^f Optical identifications from [Haggard et al. \(2009\)](#), [Cool et al. \(2013\)](#) and this work; “NV” and “V” IDs are variable stars from [Kaluzny et al. \(2004\)](#); parentheses indicate stars are non-members according to [Bellini et al. \(2009\)](#); ^g Fluxes determined using a spectrum appropriate for this object shows no change from 2000 to 2012 ([Heinke et al. 2014](#)).